

Review

Magnetic Field as an Important Tool in Exploring the Strongly Correlated Fermi Systems and Their Particle–Hole and Time-Reversal Asymmetries

Vasily R. Shaginyan ^{1,2,*} , Alfred Z. Msezane ²  and Stanislav A. Artamonov ¹

¹ Petersburg Nuclear Physics Institute, NRC Kurchatov Institute, 188300 Gatchina, Russia; artamonov_sa@pnpi.nrcki.ru

² Department of Physics, Clark Atlanta University, Atlanta, GA 30314, USA; amsezane@cau.edu

* Correspondence: vrshag@thd.pnpi.spb.ru

Abstract: In this review, we consider the impact of magnetic field on the properties of strongly correlated heavy-fermion compounds such as heavy-fermion metals and frustrated insulators with quantum spin liquid. Magnetic field B can be considered a universal tool, allowing the exploration of the physics controlling the remarkable properties of heavy-fermion compounds. These vivid properties are T/B scaling, exhibited under the application of magnetic field B and at fixed temperature T , and the emergence of Landau Fermi liquid behavior under the application of magnetic field. We analyze the influence of quasiparticle–hole asymmetry on the properties of heavy-fermion (HF) compounds such as the universal scaling behavior of the thermopower S/T exhibited under the application of magnetic field B . We show that universal scaling is demonstrated by different HF compounds such as β -YbAlB₄, YbRh₂Si₂, and strongly correlated layered cobalt oxide [BiBa_{0.66}K_{0.36}O₂]CoO₂. Analyzing YbRh₂Si₂, we show that the T/B scaling behavior of S/T is violated at the antiferromagnetic phase (AF) transition. The residual resistivity ρ_0 and the density of states N_0 experience jumps at the AF transition, causing two jumps in the thermopower and its sign reversal. Our consideration is based on the flattening of the single-particle spectrum that strongly affects ρ_0 and N_0 and leads to the violation of particle–hole symmetry. The particle–hole asymmetry generates the asymmetrical part $\Delta\sigma_d(V)$ of tunneling differential conductivity $\sigma_d(V)$, $\Delta\sigma_d(V) = \sigma_d(V) - \sigma_d(-V)$, where V is the voltage bias. We demonstrate that in the presence of magnetic field, the quasiparticle–hole asymmetry vanishes, the LFL behavior is restored, and the asymmetry disappears. Our calculations of the mentioned properties of HF compounds, based on the fermion condensation theory, are in good agreement with the experiment and support our conclusion that the fermion condensation theory is capable of describing the properties of HF compounds, including those exhibited under the application of magnetic field.

Keywords: quantum phase transition; flat bands; non-Fermi-liquid states; strongly correlated electron systems; heavy fermions; thermoelectric; thermomagnetic effects



Citation: Shaginyan, V.R.; Msezane, A.Z.; Artamonov, S.A. Magnetic Field as an Important Tool in Exploring the Strongly Correlated Fermi Systems and Their Particle–Hole and Time-Reversal Asymmetries. *Magnetism* **2023**, *3*, 180–203. <https://doi.org/10.3390/magnetism3030015>

Academic Editor: Zhe Wang

Received: 11 April 2023

Revised: 30 May 2023

Accepted: 20 June 2023

Published: 29 June 2023



Copyright: © 2023 by the authors. Licensee MDPI, Basel, Switzerland. This article is an open access article distributed under the terms and conditions of the Creative Commons Attribution (CC BY) license (<https://creativecommons.org/licenses/by/4.0/>).

1. Introduction

The Landau Fermi liquid (LFL) theory describes Fermi liquids such as ³He and electron liquids in ordinary metals. It is founded on the Landau paradigm where, at low temperatures, the properties of Fermi liquid are determined by Fermi quasiparticles. The number density x of quasiparticles coincides with that of particles in the Fermi liquid in question. Quasiparticles represent the elementary excitations of Fermi liquid, with the effective mass M^* being a parameter of the theory, weakly dependent on temperature T , magnetic field B , etc. [1–3].

The discovery of strongly correlated Fermi systems represented by heavy-fermion (HF) compounds, such as heavy-fermion (HF) metals, high- T_c superconductors, frustrated insulators with quantum spin liquid, and 2D ³He exhibiting non-Fermi liquid (NFL) behavior,

has opened a new perspective in the area of modern condensed-matter physics [4–12]. Data collected on HF compounds demonstrate that the effective mass M^* strongly depends on pressure P , T , x , B , etc., while M^* itself can extend to very high values or even diverge [7,8]. This behavior is very unusual and cannot be described within the framework of the traditional Landau quasiparticles paradigm. The common opinion suggests that quantum criticality is induced by collective fluctuations, either magnetic or superconductive. Thus, HF compounds undergo a second-order phase transition at their quantum critical point (QCP). As a result of these superconducting or magnetic fluctuations, quasiparticles are suppressed, and the NFL behavior emerges, depending on the initial ground state, either magnetic or superconductive [4,5,7,8,10]. One expects that the NFL behavior is explained within the frameworks of the spin-density-wave scenario and the unconventional Kondo-breakdown scenario (see, e.g., [7–9]). Experimental facts reveal that these scenarios are not universal since HF compounds have very different microscopic and physical structures. Moreover, some HF compounds are not located at a quantum phase transition (QPT) with possible magnetic fluctuations, while others are represented by 2D ^3He or by frustrated insulators with quantum spin liquid, which have nothing to do with fluctuations, the spin-density-wave scenario, or the Kondo effect.

The condensed-matter physics of the current millennium are vividly represented by the visiting card of the experimental discovery of flat bands (see, e.g., [11,12]) since HF compounds with flat bands are numerous [13]. Thus, one can expect the existence of a general physical mechanism facilitated by the presence of flat bands, exhibiting itself as the universal properties of HF compounds. As a result, HF compounds can demonstrate universal scaling behavior (see, e.g., [14–17]). Within the framework of the fermion condensation (FC) theory, such a mechanism is represented by the topological fermion condensation quantum phase transition (FCQPT) recreating quasiparticles, intimately related to the unlimited growth of M^* , producing NFL behavior, and generating flat bands. Further studies show that it is capable of delivering an adequate theoretical explanation of a vast majority of experimental results in different HF metals [14–24]. In contrast to the Landau paradigm, based on the assumption that M^* is a constant, in the fermion condensation theory, the effective mass M^* strongly depends on P , T , x , B , etc. As a consequence, to account for the numerous data, the extended quasiparticles paradigm should be employed. The main item here is that the well-defined quasiparticles define the thermodynamic, relaxation, and transport properties of HF compounds, making M^* become a function of T , x , B , and P , etc. [15,23,25]. We note that the well-known Kadowaki–Woods relation [26] is conserved [15], and that obvious experimental facts can hardly be explained within the framework of the spin-density-wave scenario, the unconventional Kondo-breakdown scenario, etc. The FC theory has been successfully applied to describe the thermodynamic properties of different HF compounds. Thus, the outstanding puzzle of HF compounds originating from their universal behavior, which drastically differs from the behavior of ordinary metals and superconductors, is resolved [14–17,23,25], and the fundamental physics of HF compounds are controlled by the topological FCQPT (see, e.g., [15–17,20,27]). It is plausible to probe the other properties of HF compounds, which are not directly determined by the effective mass M^* and cannot be explained within the framework of theories based on conventional quantum phase transitions (see, e.g., [15,20,24,28–31]). An important feature explained within the framework of the FC theory is the crossover from NFL behavior to LFL behavior under the application of magnetic field B , pressure P , etc. When the system in question transits under the application of magnetic field B from its NFL state to the LFL state, the impact of FC on the thermodynamic and transport properties is strongly changed. For example, the quasiparticle–hole asymmetry generating the asymmetrical part $\Delta\sigma_d(V)$ of tunneling differential conductivity $\sigma_d(V)$ vanishes, where $\Delta\sigma_d(V) = \sigma_d(V) - \sigma_d(-V)$, and where V is the voltage bias [15]. Due to the same reason, the residual resistivity $\rho_0(B)$ under the application of magnetic field B is strongly reduced, and the behavior of the resistivity $\rho(T)$ changes from $\rho(T) \propto T$ to $\rho(T) \propto T^2$ [17,32]. Moreover, the dependence of the magnetic field on the Hall coefficient $R_H(B)$ provides information about the QCP, determining the

properties of HF metals [31]. Experiments have shown that the Hall coefficient $R_H(B)$ in the antiferromagnetic HF metal YbRh_2Si_2 in magnetic fields B undergoes a jump in the zero-temperature limit under the application of magnetic field B , tuning the metal from the antiferromagnetic to the paramagnetic state at $B = B_{c0}$ [33]. The jump occurs when the magnetic field B reaches its critical value B_{c0} , at which the Néel temperature $T_N(B)$ of the antiferromagnetic transition vanishes, $T_N(B \rightarrow B_{c0}) \rightarrow 0$. The jump is interpreted as a collapse of the large Fermi surface precisely at the QCP [33]. The FC theory successfully explains this behavior as a universal one represented by the transition from the NFL state with FC to the Landau Fermi liquid (LFL) state [17,31]. Moreover, the FC state is characterized by broken \mathcal{T} and \mathcal{C} symmetries occurring at the topological FCQPT in CeCoIn_5 that connects two Fermi surfaces of different topological charges [15–17,19,20,30,31] (for detail, see Section 7.2). Recent measurements of the Hall coefficient on the prototypical superconductor CeCoIn_5 allow one to interpret the observed quantum phase transition as a delocalization quantum phase transition without symmetry breaking in CeCoIn_5 . This transition is characterized by the delocalization of f -electrons in the transition that connects two Fermi surfaces of different volumes [28]. Measurements of $\Delta\sigma_d(V)$ and $\rho_0(B)$ in the presence of the magnetic field B allow one to verify this observation.

In our review, based on important experimental facts and their explanation, we consider employing magnetic fields to reveal the physics of HF compounds. We focus on the crossover from the NFL behavior to the LFL behavior that takes place under the application of magnetic field B . This crossover is of crucial importance since at the LFL state, the quasiparticle particle–hole asymmetry generated by the FC state is eliminated. As a result, one can observe a change in the transport properties, such as the reduction of the residual resistivity $\rho_0(B)$, the vanishing of the asymmetrical part $\Delta\sigma_d(V)$ of the differential tunneling conductivity $\sigma_d(V)$, and the reduction of the thermopower S . We also analyze the Hall coefficient $R_H(B)$ and explain its behavior in HF metals under the application of magnetic field. We demonstrate that this behavior is determined by the presence of flat bands formed by the topological FCQPT. The flat band in archetypal HF metal CeCoIn_5 [34] forms its properties, while in the LFL state, the related violations of symmetries are eliminated. We show that the measured transport properties yield direct evidence of the apparent broken symmetries, such as the violation of the \mathcal{T} and \mathcal{C} symmetries occurring at the topological FCQPT in CeCoIn_5 . Analyzing the data collected in measurements of the change in the residual resistivity $\rho_0(B)$ on CeCoIn_5 , we demonstrate that the change in the Fermi surface of CeCoIn_5 is determined by the topological FCQPT, connecting two Fermi surfaces of different topological charges. We show that it is the topological FCQPT that occurs in both the archetypal HF metals CeCoIn_5 and YbRh_2Si_2 [17,31].

2. The Effective Mass M^*

We start by considering an HF liquid at $T = 0$ characterized by the effective mass M^* . Upon applying the well-known Landau equation, we relate M^* with the bare electron mass M [2,35]

$$\frac{M^*}{M} = \frac{1}{1 - N_0 F^1(x)/3}. \quad (1)$$

Here, N_0 is the density of states of a free-electron gas, $x = p_F^3/3\pi^2$ is the number density, p_F is the Fermi momentum, and $F^1(x)$ is the p -wave component of the Landau interaction amplitude F . At the critical point $x = x_c$, $F^1(x)$ reaches a certain value at which the denominator in Equation (1) vanishes. As a result, at $T = 0$, the effective mass M^* diverges, and the system is at the topological FCQPT (see, e.g., [15]). It is seen from Equation (1) that beyond the critical point x_c , the effective mass becomes negative. To prevent falling into the unstable and physically meaningless state with a negative effective mass, the system is to undergo the topological FCQPT occurring at the quantum critical

point $x = x_c$ [15,20]. The asymmetrical phase behind the quantum critical point possesses the topological charge, forms a flat band, and is determined by [18–20]

$$\frac{\delta E[n(\mathbf{p})]}{\delta n(\mathbf{p}, T = 0)} = \varepsilon(\mathbf{p}) = \mu. \tag{2}$$

The solution of Equation (2) is delivered by the occupation numbers $n_0(\mathbf{p})$ and takes place in the interval

$$0 < n_0(\mathbf{p}) < 1; \quad p_i \leq p \leq p_f. \tag{3}$$

It is seen from Equation (2) that the flat band is located in the interval $p_i < p < p_f$. Here, E is the Landau functional of the ground-state energy [2], μ is a chemical potential, and $n(\mathbf{p})$ is the occupation number of quasiparticles. The main result of such rearrangement is that instead of a Fermi step, we have $0 < n_0(p) < 1$ in a certain range of momenta $p_i \leq p \leq p_f$. Accordingly, the single-particle spectrum

$$\frac{\delta E}{\delta n(\mathbf{p})} = \varepsilon(\mathbf{p}) \tag{4}$$

in the momenta interval $(p_i - p_f)$ becomes flat, $\varepsilon(\mathbf{p}) = \mu$, and this flat spectrum is known as the FC state [18]. It is seen from Equation (3) that the occupation numbers in the interval become $0 < n_0(\mathbf{p}) < 1$, and the FC state is characterized by the superconducting order parameter $\kappa(\mathbf{p}) = \sqrt{n_0(\mathbf{p})(1 - n_0(\mathbf{p}))}$ [15].

To obtain the equation defining the effective mass M^* , we employ the density functional theory of the superconducting state [36,37]. As a result, the ground-state energy E becomes the exact functional of the occupation numbers $n(\mathbf{p})$ and the function of the number density x , $E = E[n(\mathbf{p}), x]$, while Equation (4) gives the exact single-particle spectrum $\varepsilon(\mathbf{p})$ [37]. Upon differentiating both sides of Equation (4) with respect to \mathbf{p} and after some algebra and integration by parts, we obtain

$$\frac{\partial \varepsilon(\mathbf{p})}{\partial \mathbf{p}} = \frac{\mathbf{p}}{M} + \int F(\mathbf{p}, \mathbf{p}_1) \frac{\partial n(\mathbf{p}_1)}{\partial \mathbf{p}_1} \frac{d\mathbf{p}_1}{(2\pi)^3}. \tag{5}$$

Here, $F(\mathbf{p}, \mathbf{p}_1) = \delta^2 E / \delta n(\mathbf{p}) \delta n(\mathbf{p}_1)$ is the Landau amplitude. To calculate the derivative $\partial \varepsilon(\mathbf{p}) / \partial \mathbf{p}$, we utilize the functional representation

$$E[n] = \int \frac{p^2}{2M} n(\mathbf{p}) \frac{d\mathbf{p}}{(2\pi)^3} + \frac{1}{2} \int F(\mathbf{p}, \mathbf{p}_1) n(\mathbf{p}) n(\mathbf{p}_1) \frac{d\mathbf{p} d\mathbf{p}_1}{(2\pi)^6} + \dots \tag{6}$$

It follows from Equation (5) that M^* is given by the well-known Landau equation

$$\frac{1}{M^*} = \frac{1}{M} + \int \frac{\mathbf{p}_F \mathbf{p}_1}{p_F^3} F(\mathbf{p}_F, \mathbf{p}_1) \frac{\partial n(p_1)}{\partial p_1} \frac{d\mathbf{p}_1}{(2\pi)^3}. \tag{7}$$

For simplicity, we have omitted the spin degrees of freedom. To calculate M^* as a function of T , we construct the free energy $F = E - TS_e$, where the entropy S_e is given by

$$S_e = -2 \int [n(\mathbf{p}) \ln(n(\mathbf{p})) + (1 - n(\mathbf{p})) \ln(1 - n(\mathbf{p}))] \frac{d\mathbf{p}}{(2\pi)^3}, \tag{8}$$

that follows from general combinatorial reasoning [2]. Minimizing F with respect to $n(\mathbf{p})$, we arrive at the Fermi–Dirac distribution

$$n(\mathbf{p}, T) = \left\{ 1 + \exp \left[\frac{(\varepsilon(\mathbf{p}, T) - \mu)}{T} \right] \right\}^{-1}. \tag{9}$$

Due to the employed procedure [37], we conclude that Equations (5) and (7) are exact and allow the calculation of the behavior of both $\partial\varepsilon(\mathbf{p})/\partial\mathbf{p}$ and M^* in the vicinity of the topological FCQPT, where the well-defined quasiparticles determine the low-temperature physics, while M^* becomes a function of T , B , and x . Effective mass M^* diverges at $T \propto B \rightarrow 0$ and $x \rightarrow x_c$ [15,23,25]. This feature of M^* forms the NFL behavior, and the crossover to the LFL behavior is observed in measurements on HF metals (see Figure 2a,b).

3. The Scaling of the Effective Mass

When analyzing HF compounds, we face the problem related to the anisotropy of the crystal lattice of solids, impurities, etc. This problem can be simplified, for we study the universal behavior of HF compounds based on the model of homogeneous HF liquid [15–17]. The model has a corresponding ability since we consider the universal scaling behavior exhibited by these materials at low temperatures a behavior related to the power-law divergences of quantities such as the effective mass, heat capacity, magnetization, etc. These divergences and the universal scaling of the effective mass or critical exponents that characterize them are set small compared to the Debye characteristic temperature and momentum transferred in energy and momentum on the order of the reciprocal lattice cell length a^{-1} . Therefore, quasiparticles are affected by the crystal lattice averaged over large distances compared to the length a . As a result, we can use the well-known jelly model to build a model of a homogeneous HF fluid [15–17].

In the FC theory, the QPT is interpreted as the topological FCQPT at which the quasiparticle effective mass M^* diverges. In that case, quasiparticles with energy $\varepsilon \sim \mu$ are well-defined excitations [15–17], while the FC state itself is protected by topological invariants [19,21,22]. In the vicinity of the FCQPT, in order to reveal the universal scaling behavior of M^* observed in HF compounds, it is helpful to use “internal” scales for measuring quantities such as, e.g., C/T and M^* , temperature T , etc. [15,16]. Maximum values $(C/T)_M \propto M_M^*$ in both C/T and M^* , respectively, at temperature T_M appear under the application of magnetic field B , and T_M acquires higher values as magnetic field B is elevated. To obtain $(C/T)_N$, we use $(C/T)_M$ and T_M as “internal” scales: $(C/T)_M$ is used to normalize C/T , and T is normalized by T_M [15,16]. In the same way, we normalize M^* to obtain the normalized effective mass $M_N^* = M^*/M_M^*$ as a function of the normalized temperature $T_N = T/T_M$. To study the scaling behavior of $M^*(B, T)$, we use the model of homogeneous HF liquid, which permits the avoidance of complications associated with the crystalline anisotropy of solids [2,15,16]. We write the quasiparticle distribution function as $n_1(\mathbf{p}) = n(\mathbf{p}, T) - n(\mathbf{p})$, where $n(\mathbf{p})$ is the step function, and Equation (7) then becomes [2,15,16]

$$\frac{1}{M^*(T)} = \frac{1}{M^*} + \int \frac{\mathbf{p}_F \mathbf{p}_1}{p_F^3} F(\mathbf{p}_F, \mathbf{p}_1) \frac{\partial n_1(p_1, T)}{\partial p_1} \frac{dp_1}{(2\pi)^3}. \quad (10)$$

At the FCQPT, the effective mass M^* diverges, and Equation (10) becomes homogeneous, determining M^* as a function of temperature

$$M^*(T) \propto T^{-2/3}, \quad (11)$$

while the system exhibits NFL behavior [15,16,25]. If the system is located before the topological FCQPT, M^* is finite, and at low temperatures, the system demonstrates LFL behavior such that $M^*(T) \simeq M^* + a_1 T^2$, where a_1 is a constant. The LFL regime occurs when the second term on the right-hand side of Equation (10) is small in comparison with the first term. Then, with rising temperatures, the system enters the transition regime: M^* grows, reaching its maximum M_M^* at $T = T_M$, and subsequently decreases. At $T \geq T_M$, the last “traces” of the LFL regime disappear, and the second term starts to dominate. Again, Equation (10) becomes homogeneous, and the NFL regime, manifesting itself in a decrease

in M^* as $T^{-2/3}$, is recreated. The application of magnetic field reproduces the LFL regime so that M_M^* depends on B as

$$M_M^* \propto (B - B_{c0})^{-2/3}, \quad (12)$$

while

$$T_M \propto \mu_B (B - B_{c0}), \quad (13)$$

where μ_B is the Bohr magneton [15,25]. Now, we consider the applied magnetic field B as a variable, while the temperature is fixed $T = T_f$. In that case, as seen from Equations (11) and (12), it is convenient to introduce variable $y = (B - B_{c0})/T$ and rewrite Equation (13) as [15]

$$y = T_N = \frac{T}{T_M} \propto \frac{T}{\mu_B (B - B_{c0})}. \quad (14)$$

Near the topological FCQPT, the normalized solution of Equation (10) $M_N^*(T_N)$ can be well approximated by a simple universal interpolating function [15,16]. The interpolation occurs between the LFL ($M^* \simeq M^* + a_1 T^2$) and NFL ($M^* \propto T^{-2/3}$) regimes, describing the above crossover and representing the universal scaling of M_N^* [15,16,25]

$$M_N^*(y) \approx c_0 \frac{1 + c_1 y^2}{1 + c_2 y^{8/3}}. \quad (15)$$

Here, y is given by Equation (14), and $c_0 = (1 + c_2)/(1 + c_1)$, c_1 , and c_2 are fitting parameters. Magnetic field B enters Equation (10) only in the combination B/T , resulting in Equation (14). Thus, in the presence of a fixed magnetic field, the variable y becomes $y = T/T_M = (T/(B - B_{c0}))_N \sim T/(B - B_{c0})$. Here, $(T/(B - B_{c0}))_N$ is the normalized value of $T/(B - B_{c0})$; it is calculated in the same way as it is in the case of T_N .

Thus, Equation (15) describes the universal scaling of M_N^* as a function of T versus B . The curves M_N^* at different magnetic fields B merge into a single curve in terms of the normalized variable $y = T/T_M$. The universal scaling of $(C/T)_N = M_N^*$ extracted from measurements of C/T under the application of magnetic field of the archetypal HF metal YbRh_2Si_2 [38] is shown in Figure 1. The solid theoretical curve coincides with that shown in Figure 2b. Equation (15) describes the scaling of $M_N^*(B, T)$ as a function of B versus T [2,15,16]. It is seen in Figure 1 that there are deviations between the theoretical curve and the normalized experimental data at $T_N \geq 7$, which can possibly come from our normalization of the experimental data. The deviation can also emerge due to the subtraction procedure of the contribution of the phonon to the electronic specific heat of YbRh_2Si_2 [38] at relatively high temperatures.

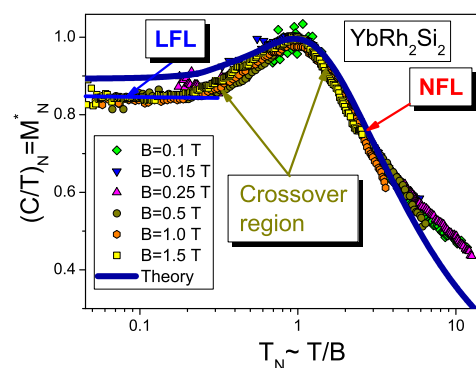


Figure 1. Universal scaling behavior of the normalized specific heat $(C/T)_N$ as a function of the normalized temperature T_N . $(C/T)_N$ is obtained from measurements of the heat capacity C/T at YbRh_2Si_2 in magnetic fields B [38] depicted in the legend. The LFL region, crossover region, and NFL region are displayed by the arrows. The solid curve represents our calculations of $(C/T)_N = M_N^*$ based on Equations (10) and (15) (see Figure 2b) [15].

A schematic phase diagram of HF metal is shown in Figure 2a. Magnetic field B is taken as the control parameter. In fact, the control parameter can be pressure P or doping (the number density) x , etc., as well. At $B = B_{c0}$, FC occurs, leading to a strongly degenerated state, where B_{c0} is a critical magnetic field such that, at $B > B_{c0}$, the system is driven towards its Landau Fermi liquid (LFL) regime. In our simple model, B_{c0} is a parameter. The FC state is captured by the superconducting (SC), ferromagnetic (FM), antiferromagnetic (AFM), etc., states lifting the degeneracy [15,23]. Below, we consider the archetypal HF metal YbRh_2Si_2 (see also Section 5). In this case, $B_{c0} \simeq 0.06 \text{ T}$ ($B \perp c$), and at $T = 0$ and $B < B_{c0}$, the AFM state takes place at $T < T_{NL}(B)$ [39]. At elevated temperatures and a fixed magnetic field, the NFL regime occurs, while rising B again drives the system from the NFL region to the LFL region, as shown by the dashed-dotted horizontal arrow in Figure 2. Figure 2b demonstrates the universal scaling of the normalized effective mass $M_N^* = M^*/M_M^*$ versus normalized temperature $T_N = T/T_M = (T/B)_N$, where M_M^* is the maximum value that M^* reaches at $T = T_M$. The $T^{-2/3}$ regime is marked as an NFL regime since the effective mass depends strongly on temperature. The temperature region $T \simeq T_M$ signifies the crossover between the LFL regime with almost constant effective mass and NFL behavior, given by $T^{-2/3}$ dependence. Thus, the region $T \sim T_M$ can be considered the crossover region taking place between the LFL and NFL regimes. From Equation (15), it follows that, in contrast to the Landau paradigm of quasiparticles, the effective mass $M^*(T, B)$ strongly depends on both temperature T and magnetic field B . We note that such a dependence $M^*(T, B)$ forms both the crossover region and the NFL region. It is also seen from Equation (15) that the scaling behavior of $M_N^*(T/B)$ near the topological FCQPT is formed by the absence of appropriate external physical scales to measure the effective mass and temperature. At fixed magnetic fields, the characteristic scales of the temperature and of the function $M^*(T, B)$ are defined by both T_M and M_M^* , respectively. At fixed temperatures, the characteristic scales are $(B_M - B_{c0})$ and M_M^* . Here, B_M is the magnetic field at which occurs the maximum M_M^* of the effective mass. From Equations (12) and (13), it follows that at $T \simeq 0$ $T_M \rightarrow 0$, $M_M^* \rightarrow \infty$, and the width of the transition region shrinks to zero as $B \rightarrow B_{c0}$. In the same way, it is seen from Equations (11) and (14) that at a fixed magnetic field $(B - B_{c0}) \simeq 0$, the maximum value $M_M^* \rightarrow \infty$ and the width of the transition region shrinks to zero as $T \rightarrow 0$.

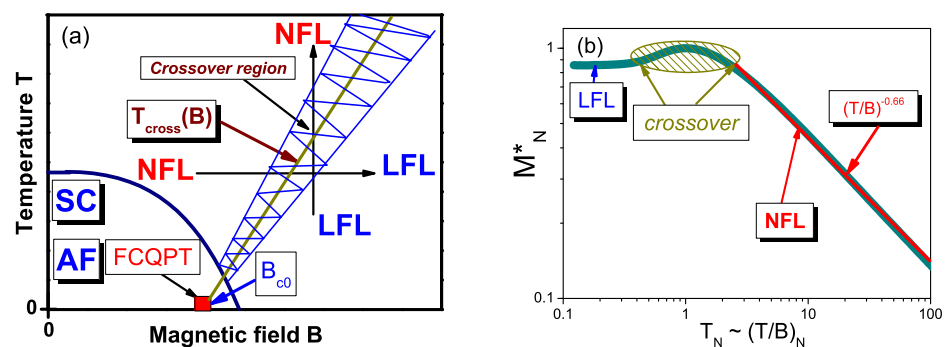


Figure 2. Panel (a): Schematic phase diagram of HF metals. B_{c0} is magnetic field at which the effective mass diverges. SC and AF denote the superconducting (SC) and antiferromagnetic (AFM) states, respectively. At $B \lesssim B_{c0}$, the system can be captured by AFM or SC states. The vertical arrow depicts the transition from the LFL regime to the NFL regime at fixed B . The horizontal arrow illustrates the HF metals in question transiting from the NFL to the LFL regime along B at fixed T . Panel (b) displays the schematic plot of the universal scaling behavior of the normalized effective mass M_N^* versus the normalized temperature $T_N \propto (T/B)_N$. The crossover region, where M_N^* reaches its maximum value M_M^* at $T = T_M$, is shown by the hatched area. The system transits from the NFL to the LFL behavior at rising B at fixed T , which is at $T/B < 1$. The arrows mark the LFL and the NFL regions and the transition region in the behavior of M_N^* as a function of $T_N = (T/B)_N$. The NFL behavior is characterized by $M^* \propto (T/B)^{-2/3} \simeq (T/B)^{-0.66}$ (see Equation (12)).

It is seen in Figure 3 that the universal scaling behavior of the thermodynamic properties stems from the fact that HF compounds are located near the topological FCQPT, generating flat bands [15,16]. As an example, Figure 3a displays universal B/T scaling for over more than three orders, demonstrated by $T^{2/3}\chi$ of the HF metal $\text{CeCu}_{6-x}\text{Au}_x$ and of the frustrated insulator herbertsmithite $\text{ZnCu}_3(\text{OH})_6\text{Cl}_2$. Here, χ is the magnetic susceptibility. Since the effective mass $M^*(T)$ diverges, $M^*(T) \propto T^{-2/3}$ (see Equation (11)), $T^{2/3}\chi \propto \text{const}$, as seen in Figure 3a. It is seen in Figure 3b that the normalized magnetic specific heat $(C_{\text{mag}}/T)_N$ exhibits scaling in a wide range of the variable $(T/B)_N$. The observed universal scaling exhibited by HF compounds represents a convincing example of the influence of magnetic field on the properties of the system, allowing the exploration of its universal properties. Data are extracted from Refs. [40–42]. The existence of such universal behavior, exhibited by various and very distinctive strongly correlated Fermi systems, supports the conclusion that HF compounds represent a new state of matter [15–17]. In contrast to the situation for an ordinary quantum phase transition, this scaling, induced by the topological FCQPT, occurs up to relatively high temperatures $T \sim 100$ K since the NFL behavior is defined by quasiparticles with M_N^* given by Equation (15), rather than by fluctuations or Kondo lattice effects [15,16].

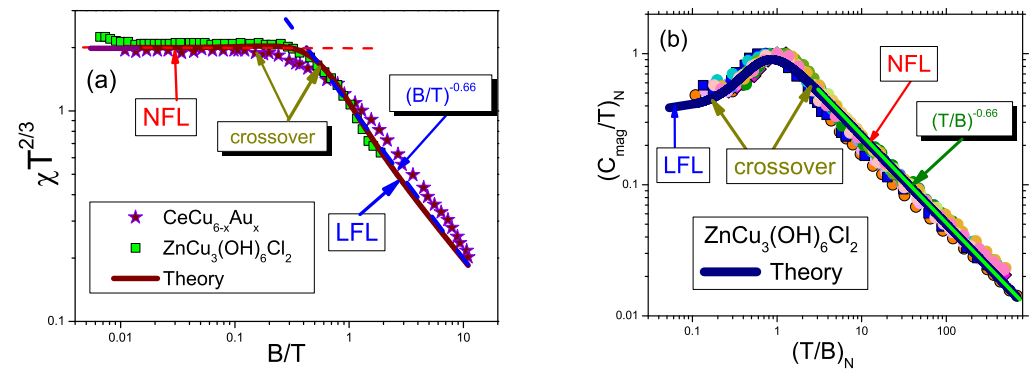


Figure 3. Universal B/T scaling of thermodynamic properties of strongly correlated Fermi systems. Panel (a): Scaling of magnetic susceptibility $\chi T^{2/3}$ of the HF metal $\text{CeCu}_{6-x}\text{Au}_x$. Data are extracted from experimental measurements [40], and that of $\text{ZnCu}_3(\text{OH})_6\text{Cl}_2$ from data [41]. At $B/T \ll 1$ m the systems exhibit NFL behavior with $\chi \propto M^*$, as given by Equation (11), i.e., $T^{2/3}\chi \propto \text{const}$. At $B/T \gg 1$, the systems demonstrate LFL behavior, with χ as given by Equation (12), being a decreasing function of B/T (see Equation (15)). Panel (b): T/B scaling of the specific heat C_{mag}/T of $\text{ZnCu}_3(\text{OH})_6\text{Cl}_2$ is extracted from data [42]. At $T/B \ll 1$, the systems demonstrate LFL behavior with $\chi \propto \text{const}$. At $T/B > 1$, the systems exhibit NFL behavior with $\chi \propto T^{2/3}$.

4. Flat Bands and Particle–Hole Asymmetry

Experimental facts show that the particle–hole asymmetry exists in HF compounds and is accompanied by Fermi surface transformation [43–45]. Such behavior is illuminated by the strong enhancement of the observed low-temperature value of the Seebeck coefficient [43–45]. The measurements on twisted bilayer graphene also confirm the strong particle–hole asymmetry that leads to the thermopower generation, so the Seebeck coefficient reaches high values of an order of magnitude larger than in common metals exhibiting LFL behavior. Both the observed asymmetry and the strong Seebeck coefficient enhancement were predicted about thirty years ago and determined by FC, forming flat bands [20]. As soon as the electronic system of the HF compound approaches the threshold of the topological FCQPT, the dispersion of an electronic quasiparticle disappears in some part of its spectrum, forming flat bands [15,16]. This dispersionless part is usually situated between momentum p_i (standing for initial momentum) and p_f (final momentum) (see Equation (2)). Clearly, in this dispersionless part of the spectrum, the effective mass M^* diverges. Beyond the topological FCQPT, FC is formed so that the step quasiparticle distribution function $n_F(p, T \rightarrow 0) = \theta(p - p_F)$ does not minimize the Landau functional

$E[n(\mathbf{p})]$, and the quasiparticle distribution is determined by Equation (2) for the minimum of the functional. At $T = 0$, Equation (2) determines the quasiparticle distribution function $n_0(\mathbf{p})$, minimizing the ground-state energy $E \equiv E[n(\mathbf{p})]$. Figure 4 reports a typical $n_0(\mathbf{p})$, with E_F being the Fermi energy. It is seen in Figure 4 that the particle–hole symmetry is violated by FC since $n_0(\mathbf{p})$ does not evolve from the Fermi–Dirac distribution function, a step at $T = 0$, shown by the blue line. In Figure 4, the arrow shows the hole states formed by the FC. As we will see in Sections 5.2 and 7.2, as soon as the flat band is eliminated under the application of magnetic field, the asymmetry vanishes, and the thermopower is strongly diminished, while the residual resistivity ρ_0 strongly diminishes (see Section 7.1), and the asymmetrical part $\Delta\sigma_d(V)$ of the tunneling conductivity disappears (see Section 7.2). These observations shed light on the role of the magnetic field B and strongly support the FC theory, explaining the emergence of the particle–hole asymmetry and the corresponding experimental facts collected on HF metals and graphene.

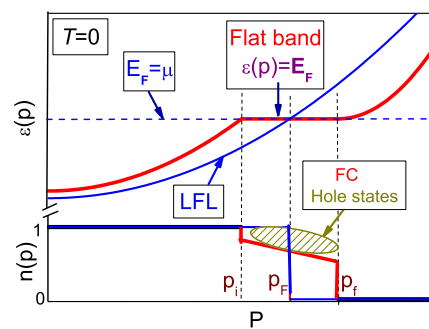


Figure 4. The single-particle energy $\varepsilon(\mathbf{p})$ and the distribution function $n(\mathbf{p})$ at $T = 0$. The arrow shows the Fermi energy $E_F = \mu$. The vertical lines denote the FC area $p_i < p < p_f$ with $0 < n_0(p) < 1$ and $\varepsilon(\mathbf{p}) = E_F$. The Fermi momentum p_F is in the interval $p_i < p_F < p_f$ and corresponds to the Landau Fermi liquid, emerging when the FC state and the corresponding particle–hole asymmetry are eliminated. The single-particle energy $\varepsilon(\mathbf{p})$ and distribution function $n(\mathbf{p})$ of the LFL state are displayed by the blue lines. The arrow indicates the hole states generated by the flat band.

5. Thermopower under the Application of Magnetic Fields

The study of the thermopower S/T in HF metals and graphene reveals a strong interaction driven particle–hole asymmetry [43–45]. In this section, we make use of data collected on the archetypal HF YbRh_2Si_2 in measurements of the thermopower [46,47] to illustrate the particle–hole asymmetry and its behavior in magnetic fields. Thermopower S/T is a sensitive and helpful tool to analyze the quasiparticle excitations at the Fermi surface. Thus, we face an important problem related to revealing the scaling of the thermopower S/T , which permits the analysis of the nature of quasiparticle (electronic) excitations at the Fermi surface. In this direction, we will elucidate the role of quasiparticles and the nature of the topological FCQPT that forms the flat bands and both the particle–hole asymmetry and the behavior of the thermopower S/T in different HF compounds. We show that the thermopower S/T of YbRh_2Si_2 exhibits scaling that coincides with that of other thermodynamic functions such as $(C/T)_N$. We demonstrate that S/T of different HF compounds such as YbRh_2Si_2 , $\beta\text{-YbAlB}_4$, and $[\text{BiBa}_{0.66}\text{K}_{0.36}\text{O}_2]\text{CoO}_2$ exhibit universal scaling, determined by the scaling behavior of the effective M_N^* shown in Figures 1, 2b and 5. Using YbRh_2Si_2 as an example, we also demonstrate that the universal behavior of S/T is violated at the AF phase transition, while the residual resistivity ρ_0 and the density of states N_0 experience downward jumps at the AF phase transition that are accompanied by the restoration of the particle–hole symmetry. The restoration of the particle–hole symmetry leads to the corresponding downward jumps Jump_F of S/T that strongly diminishes and changes its sign, as seen in Figure 6. This first jump, occurring at $T \leq 0.03$ K, is shown in Figure 6 and is labeled Jump_F . It is accompanied by a change in sign of $(S/T)_N$, becoming positive [46,47]. This behavior occurs as the system undergoes the AF phase transition

taking place at T_{NL} . This first jump Jump_F reflects the elimination of both the hole state and the flat band in YbRh_2Si_2 (see Figure 4) [15–17].

5.1. Scaling

As we shall see, an analysis of the thermoelectric power S/T delivers new knowledge of the nature of quantum phase transition defining the NFL behavior of the corresponding HF compounds. For example, one reasonably proposes that S/T distinguishes between the two possible scenarios for HF metals, namely the spin-density-wave theory and the breakdown of the Kondo effect [48,49]. Indeed, S/T is sensitive to the derivative of the density of electronic states N_0 and to the change in the relaxation time τ at μ [3,50]. It follows from the Boltzmann equation that S/T can be written as [3,50–53]

$$\frac{S}{T} = -\frac{\pi^2 k_B^2}{3e} \left[\frac{\partial \ln \sigma(\varepsilon)}{\partial \varepsilon} \right]_{\varepsilon=\mu}, \quad (16)$$

where k_B and e are, respectively, the Boltzmann constant and the electron's charge, while σ is the dc electric conductivity of the system:

$$\sigma(\varepsilon) = 2e^2 \tau(\varepsilon) \int \delta(\mu - \varepsilon(\mathbf{p})) v(\mathbf{p}) v(\mathbf{p}) \frac{d\mathbf{p}}{(2\pi)^3}, \quad (17)$$

\mathbf{p} is the wave vector of the electron, and v is its velocity. It is seen from Equation (17) that S/T depends on the derivative of the density of electronic states $N_0(\varepsilon = \mu)$ and the change in the relaxation time at $\varepsilon = \mu$. Within the framework of the Fermi liquid theory, the term in the brackets on the right-hand side of Equation (16) can be simplified. As a result, one obtains $S/T \propto N(\varepsilon = \mu) \propto C/T \propto M^*$ at $T \rightarrow 0$ [50–53]. Taking into account that the charge and heat fluxes at low temperatures are transferred by quasiparticles, the S/C ratio has the form

$$(S/C) \simeq (S/S_{ent}) \simeq \text{const}. \quad (18)$$

Here, S_{ent} is the entropy density of charge carriers [50–53]. It is seen from Equation (18) that $S/T \propto M^*$. Thus, within the FC theory, which proposes the universal scaling behavior of M^* (see Section 3), one can obtain a reliable description of the thermopower and its universal scaling behavior [15–18,20,54,55].

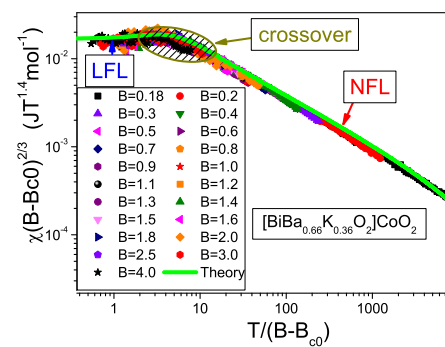


Figure 5. Scaling of the susceptibility $\chi(B - B_{c0})$ as a function of scaled temperature $T/(B - B_{c0})$ with $B_{c0} = 0.176$ T for various B values obtained in measurements on $[\text{BiBa}_{0.66}\text{K}_{0.36}\text{O}_2]\text{CoO}_2$ (see the legend [56]). The LFL region, crossover region, and NFL region are shown by the arrows. The solid curve represents our calculations based on Equation (10), and describes the universal scaling behavior $(C/T)_N = M_N^* \propto \chi(B - B_{c0})$ shown in Figure 2b.

Indeed, Figure 1 demonstrates the normalized specific heat $(C/T)_N$ as a function of T_N measured on YbRh_2Si_2 . The behavior of $(C/T)_N$ coincides with that of the magnetic susceptibility $\chi \propto C/T \propto M^*$ obtained in measurements on $[\text{BiBa}_{0.66}\text{K}_{0.36}\text{O}_2]\text{CoO}_2$ [56] and shown in Figure 5. The solid curve in Figure 5 demonstrates results of the

same calculations based on Equation (10), describing the universal scaling behavior $(C/T)_N(T/T_M) = M_N^*(T/T_M) \propto \chi(B - B_{c0})^{0.6}$ shown in Figure 1. As a result, we conclude that the solid curve drawn in both Figures 1 and 5 exhibits the universal scaling intrinsic to HF compounds [15–17].

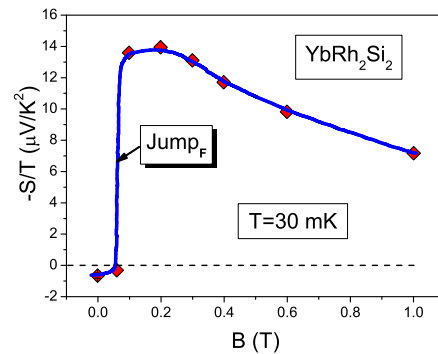


Figure 6. Thermopower isotherm $-S(B)/T$ for different temperatures given in the legend [46,47]. The label Jump_F represents the first downward jumps in $-S(B)/T$ shown by the arrows. The solid line is a guide to the eye.

As seen in Figure 7, in the case of YbRh_2Si_2 and at $T \geq T_{NL}$, the normalized isotherms $(S(B)/T)_N$ behave such as $(C/T)_N$ (see Figure 1). They demonstrate a broad maximum, which sharpens and shifts towards smaller fields upon cooling [46,47]. It is seen in Figure 6 that the above-mentioned behavior is violated as the system approaches the AF phase transition. Here, $T_{NL}(B)$ is the temperature of antiferromagnetic (AF) ordering, with $T_{NL}(B = 0) = 70$ mK, and $T_{NL}(B = B_{c0}) = 0$ at the critical field $B_{c0} = 60$ mT, applied perpendicular to the magnetically hard *c* axis [57]. Thus, outside of the AF region, $S/T \propto C/T \propto \chi \propto M^*$ over a wide range of *T* and *B* since in the framework of FC theory, the particle–hole symmetry is violated [15–17]. It is worth noting that $S/T \propto M^*$ in a poorly ordered two-dimensional electron system in silicon and tends to diverge at a finite disorder-independent density [58].

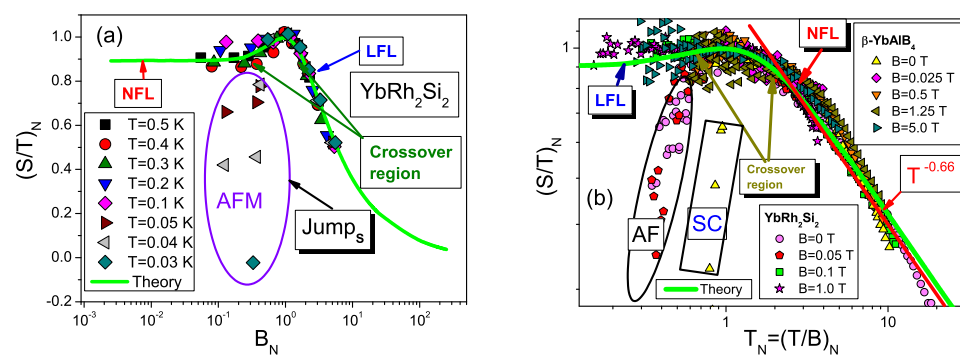


Figure 7. Universal scaling behavior of the normalized $(S/T)_N$. (a) Normalized isotherm $(S(B)/T)_N$ as a function of normalized magnetic field B_N at different temperatures *T* displayed in the legend. Outside the antiferromagnetic phase, the data show the universal scaling behavior. (b) The normalized thermopower $(S/T)_N$ in magnetic fields *B* depicted in the legend. The experimental data are extracted from measurements on YbRh_2Si_2 [46,47] and on $\beta\text{-YbAlB}_4$ [59]. The data, taken at the AF phase [46,47] and at the superconducting one (SC) [59] (delineated by the ellipse and the rectangle, respectively) expose the violation of the scaling. The theoretical solid curves in (a,b) coincide with that shown in Figures 2b and 5 [15,54].

To elucidate the scaling of the thermopower $S/T \propto C/T \propto M^*$, we normalize S/T in the same way as in the normalization of C/T (see Section 3 and Figure 1). Taking into account that $S/T \propto C/T$ [51–54], we conclude that $(S/T)_N = (C/T)_N = M_N^*$, provided

that the system in question is located away from possible phase transitions that eliminate the particle–hole asymmetry. This function $(C/T)_N = M_N^*$ is displayed in Figure 5. Figure 7a,b report $(S/T)_N$ as a function of the normalized magnetic field B_N and T_N , respectively. In Figure 7a, the function $(S/T)_N$ is obtained by normalizing (S/T) by its maximum, occurring at B_M , and the field B is scaled by B_M . As seen from Equation (15) and Figure 7a, the LFL regime sets in at $B_N > 1$ since $(S/T)_N = M_N^*$, and $M_N^* \propto (B - B_{c0})^{-2/3}$ are T -independent, while at $B_N < 1$, M_M^* becomes T -dependent and exhibits NFL behavior with $M_N^* \propto T_N^{-2/3}$. As seen in Figure 7a,b, the theoretical curves representing the universal function M_N^* (see Figures 1 and 2b) are in good agreement with the corresponding data over the wide range of B_N and T_N . Thus, $(S/T)_N = (C/T)_N = M_N^*$ exhibits the universal scaling over a wide range of its scaled variables B_N and T_N . Figure 7a also displays the scaling violation at the AF phase, when $B \leq B_{c0}$. It is seen in Figures 6 and 7a,b that the scaling is violated at $T \leq T_{NL}$ by the two downward jumps. The second jump, shown in Figure 7a and marked as Jump_S , occurs at $T_{NL} > T > 0.3$ K, while the first, taking place at $T \leq 0.03$ K, is shown in Figure 6 as Jump_F . The latter is accompanied by a change in the sign of $(S/T)_N$, which now becomes positive [46,47]. Below, we shall see that the two jumps reflect the presence of a flat band at μ in the single-particle spectrum $\varepsilon(\mathbf{p})$ of HF in YbRh_2Si_2 [15–17]. As seen in Figure 7b, scaling is violated in the same way by the superconducting (SC) phase transition, occurring in $\beta\text{-YbAlB}_4$ at $T_c \simeq 80$ mK [59].

It is worth noting that the universal scaling of $(S/T)_N$ is seen in the experimental data on the thermopower for $[\text{BiBa}_{0.66}\text{K}_{0.36}\text{O}_2]\text{CoO}_2$ [56]. The solid curve, representing our theory in Figure 8, is the same as that displaced in Figure 5, and describes $(C/T)_N$ extracted from measurements on the archetypal HF metal YbRh_2Si_2 (see Figure 1 [15]). The universal scaling behavior, and the three regimes are seen in Figure 8. These regimes are in good agreement with those reporting the universal behavior displayed in Figures 2b, 5 and 7a,b.

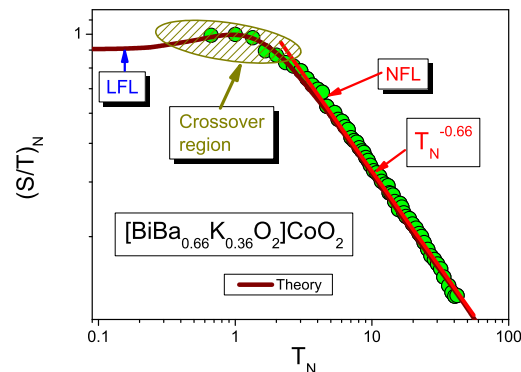


Figure 8. Scaling of S/T . At magnetic field $B = 0$, the strongly correlated layered cobalt oxide $[\text{BiBa}_{0.66}\text{K}_{0.36}\text{O}_2]\text{CoO}_2$ demonstrates the scaling of $(S(T)/T)_N$ versus T_N . The data are extracted from measurements on $[\text{BiBa}_{0.66}\text{K}_{0.36}\text{O}_2]\text{CoO}_2$ [56]. The solid curve displaying the theoretical calculations is the same as that shown in Figure 5.

5.2. Flat Bands and S/T Jumps in the AF Phase Transition

As seen in Figure 4, the ground states of systems with flat bands are degenerate. As a result, the occupation numbers $n_0(\mathbf{p})$ of single-particle states belonging to the flat band are given by a continuous function on the interval $[0, 1]$. This behavior of the occupation numbers leads to the emergence of the particle–hole asymmetry, occurring in contrast to the LFL restriction to occupation numbers 0 and 1, resulting in the particle–hole symmetry [2]. Thus, the FC state generates the entropy excess

$$S_0 = - \sum n_0(\mathbf{p}) \ln n_0(\mathbf{p}) + (1 - n_0(\mathbf{p})) \ln(1 - n_0(\mathbf{p})). \quad (19)$$

The excess S_0 does not contribute to the specific heat $C(T)$. The existence of S_0 contradicts the Nernst theorem. To avoid the violation of the Nernst theorem, FC must

be absorbed by a phase transition at $T \rightarrow 0$. For example, it can be the AF transition that becomes of the first order at some tricritical point occurring at $T = T_{tr}$ (see Section 6) [15–17]. Such a first-order phase transition eliminates the flat portion in the single-particle spectrum. Therefore, at this first-order phase transition, both the high density of states generated by the flat band and the hole states, shown by the arrow in Figure 4, vanish discontinuously, while both the occupation numbers $n_0(\mathbf{p})$ and the spectrum $\varepsilon(\mathbf{p})$ represent the LFL state, as shown by the arrows in Figure 7a. In the same way, the Fermi sphere undergoes an abrupt change, related to the first-order phase transition [15], in the interval from the momentum p_i to p_f , so as to nullify both the swelling of the Fermi surface, the entropy excess S_0 , defining the entropy S_{ent} at low temperatures, and the particle–hole asymmetry. This is a vivid example of the influence of magnetic field, which drives the AF phase transition and allows the exploration of the properties of the system. As a result, the thermopower given by Equation (18) experiences Jump_F, as it follows from Equation (19), for the entropy S_0 abruptly nullifies, while both the flat band and the particle–hole asymmetry vanish. We note that the jump is observed in the behavior of the low- T Hall coefficient of the HF metal YbRh₂Si₂ [15,16,57,60].

It is seen in Figure 6 that at $T = 0.03$ K, S/T abruptly changes its sign (the first jump—Jump_F) because the hole states are eliminated. The positive sign of S/T of YbRh₂Si₂ without the hole states [52] corresponds to the positive thermopower of its nonmagnetic counterpart LuRh₂Si₂, which has no the $4f$ hole states at the chemical potential μ [46,47,61]. Contrarily, at $T_{NL} > T > T_{cr}$, the AF phase transition is of the second order, and the entropy is a continuous function at the border of the phase transition. Thus, during a second-order phase transition, both the occupation numbers and the spectrum remain the same and retain their FC-like shape, while the system with FC is destroyed, turning into HF liquid. This destruction generates the second jump Jump_S, shown in Figure 7. As a result, the FC state is destroyed and its contribution, ρ_0^{FC} , to the residual resistivity ρ_0 vanishes, resulting in a change in the scattering time $\tau(\varepsilon = \mu)$. We note that in the presence of FC, the residual resistivity is represented by two terms $\rho_0 = \rho_0^{FC} + \rho_0^{imp}$ (see Section 7.1). Here, the residual resistivity ρ_0^{FC} is formed by the flat band generated by the FC state, while the resistivity ρ_0^{imp} is generated by impurities [16,32]. Therefore, the thermopower experiences the second jump Jump_S, as seen from Equations (16) and (17). The first downward jump Jump_F under decreasing B , defined by elimination of both ρ_0^{FC} and the hole states, is deeper than the second jump Jump_S and leads to the change in the sign of S/T . This is consistent with the experimental observations, as seen in Figures 6 and 7.

6. The Tricritical Point in the $B - T$ Phase Diagram of YbRh₂Si₂

The Landau theory of the second-order phase transitions is valid near the tricritical point, occurring at $T \simeq T_{cr}$. In that case, the fluctuation theory generates only the logarithmic corrections to the values of the critical indices [62]. Upon using the Landau theory, we obtain that the Sommerfeld coefficient $\gamma_0 = C/T$ takes the form $\gamma_0 \propto |t - 1|^{-\alpha}$, where $t = T/T_{NL}(B)$ with the exponent being $\alpha \simeq 0.5$ as the tricritical point is approached at fixed magnetic field B [17,62,63]. As seen in Figure 9, the value $\alpha = 0.5$ gives a good description of the data collected in measurements of the specific heat on YbRh₂Si₂ [63]. Taking into account that the specific heat capacity increases during the transition from the symmetric AF phase to the asymmetric one [62], we obtain

$$\gamma_N = \frac{\gamma_0(t)}{A_1} = 1 + \frac{B_1}{A_1 \sqrt{|t - 1|}}. \quad (20)$$

Here, $B_1 = B_{\pm}$ are the proportionality factors which are different for the two sides of the phase transition. The parameters $A_1 = A_{\pm}$, related to the corresponding specific heat $(C/T)_{\pm}$, are also different for the two sides, and “+” stands for $t > 1$, while “−” stands for $t < 1$.

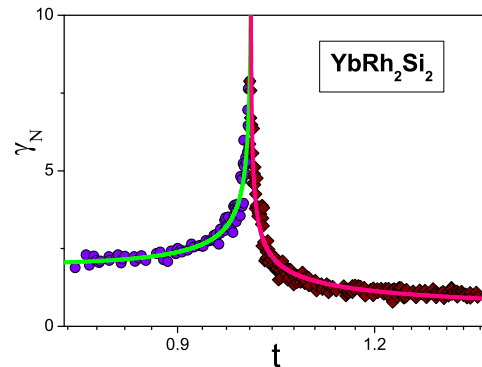


Figure 9. The normalized Sommerfeld coefficient $\gamma_N = \gamma_0/A_{\pm}$ as a function of the normalized temperature $t = T/T_{N0}$. The Sommerfeld coefficient γ_0 is given by Equation (20) and shown by the solid curves. The normalized Sommerfeld coefficient is extracted from the data obtained during measurements on YbRh₂Si₂ at the AF phase transition [63] and is represented by geometric figures.

The fit to the data for $\gamma_0 = C(T)/T$ in YbRh₂Si₂ at the AF phase transition in zero magnetic fields [63] is displayed in Figure 9. We show there the normalized Sommerfeld coefficient γ_0/A_+ as a function of the normalized temperature $t = T/T_{N0}$. It can be seen that the normalized Sommerfeld coefficient γ_0/A_+ extracted from C/T measurements at YbRh₂Si₂ [63] are well described over the entire temperature range around the antiferromagnetic phase transition by the formula (20) with $A_+ = 1$. Now, transform Equation (20) to the form

$$\gamma_{norm} = \frac{\gamma_0(t) - A_1}{B_1} = \frac{1}{\sqrt{|t-1|}}. \quad (21)$$

It follows from Equation (21) that the ratios γ_{norm} for $t < 1$ and $t > 1$ versus $|1-t|$ collapse into a single line on a double logarithmic plot. The ratios extracted from the data [63] are shown in Figure 10, the coefficients A_1 and B_1 are taken from fitting γ_N shown in Figure 7. As seen in Figure 10, the ratio γ_{norm} collapses into the single line.

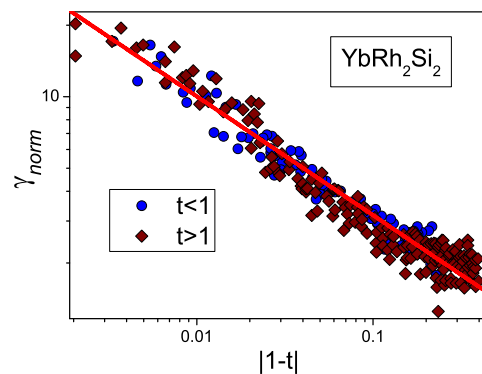


Figure 10. The temperature dependence of the ratios $\gamma_{norm} = (\gamma_0 - A_1)/B_1$ for $t < 1$ and $t > 1$ as a function of $|1-t|$ given by Equation (21) is shown by the solid line. The ratios are extracted from the data obtained in measurements of γ_0 on YbRh₂Si₂ at the AF phase transition [63] and are shown as triangles, as shown in the legend.

Based on the fits to the data, given by Functions (20) and (21) (with the critical exponent $\alpha = 1/2$) and shown in Figures 9 and 10, we predict that the AF phase transition of the second order in YbRh₂Si₂ goes into the first order under the action of a magnetic field [17]. As seen in Figure 9, the peak is sharp, while one expects that the anomalies in the specific heat related to the onset of magnetic order are to be broad [63]. Thus, the observed behavior demonstrates that the second-order phase transition is changed to the first-order phase transition at the tricritical point (see Figure 11).

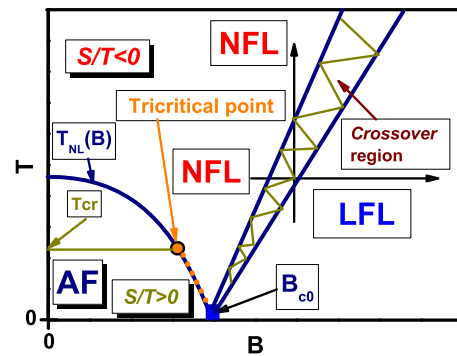


Figure 11. Schematic $T - B$ phase diagram of YbRh_2Si_2 . Vertical and horizontal arrows crossing the transition region marked with thick lines show LFL-NFL and NFL-LFL transitions at fixed B and T , respectively. The hatched area represents the crossover between the NFL and LFL regimes. As shown by the solid curve, at $B < B_{c0}$, the system is in the AF state and exhibits LFL behavior [57]. The AF phase transition line is designated $T_{NL}(B)$. The tricritical point marked with the arrow is at the point $T = T_{cr}$. At $T < T_{cr}$ the AF phase transition becomes of the first order, and is depicted by the orange dots.

Schematic $T - B$ Phase Diagram

Now, we construct the schematic $T - B$ phase diagram of the HF metal YbRh_2Si_2 (see Figure 11). In Figure 11, the NFL region formed by the state FC is characterized by an excess of entropy S_0 , defined by Equation (19). The border separating the AF state from the NFL region is shown by the solid curve $T_{NL}(B)$. At $B < B_{c0}$ and $T < T_{NL}(B)$, the system is in its AF state and exhibits LFL behavior [57]. The tricritical point T_{cr} at which the AF phase transition becomes of the first order is shown by the arrow. At that phase transition, the thermopower experiences the jump Jump_F shown in Figure 6, changes its sign, and becomes $S/T > 0$, for the hole states shown in Figure 4 are eliminated at $T < T_{cr}$. At $T > T_{cr}$, the AF transition is of the second order, and the thermopower experiences Jump_S (see Figure 6) in the NFL region $S/T > 0$, as seen in Figure 11. It is seen from the phase diagram Figure 11, that outside the area of the AF phase transition the $S_N = M_N^*$, considered a function of the dimensionless variable T_N or B_N , has the universal scaling behavior. Figures 5, 7a,b and 8 demonstrate that all the data extracted from measurements on YbRh_2Si_2 , $\beta\text{-YbAlB}_4$, and $[\text{BiBa}_{0.66}\text{K}_{0.36}\text{O}_2]\text{CoO}_2$, collapse on the single scaling curve shown in Figure 5.

Here, it is worth noting a few remarkable points. As it follows from Figures 5 and 7b, at $T_N < 1$, the normalized thermopower $(S/T)_N$ becomes constant, thus exhibiting LFL behavior. However, at $T_N \simeq 1$, the system enters the crossover region. At growing temperatures and fixed magnetic field B , NFL behavior prevails. At low temperatures and growing B and at the tricritical point, the line of the second-order phase transitions changes to the line of the first-order phase transitions, as shown by the circle in Figure 11. The same change in the phase transition occurs in the archetypal HF metals CeCoIn_5 under the application of magnetic fields $B > B_{c2} \geq B_{c0}$, where B_{c2} is the critical field destroying the superconducting state, and B_{c0} is the critical field at which the topological FCQPT takes place [17,64]. This observation allows us to conclude that at lower temperatures and under the application of magnetic field B , the curve of any second-order phase transition passes into the curve of the first-order curve at the tricritical point T_{cr} (see Figure 11). Such a behavior occurs since, at T_{cr} the entropy S_e starts to experience a jump because of the residual entropy S_0 , occurring at the NFL state and given by Equation (19), is absent in the ordered state [15]. Thus, we again underline the important role of the magnetic field in the study of the properties of HF compounds.

7. Magnetic Field to Probe the Nature of Quantum Phase Transition

In this section, we show how to utilize magnetic field when probing a quantum phase transition that forms the properties of an HF metal. As an example, we consider the archetypal HF metal CeCoIn₅.

The condensed-matter community is involved in active debate on the nature of the quantum phase transition (QPT) governing the low-temperature properties of heavy-fermion (HF) metals. Recent experimental observations of the archetypal HF metal CeCoIn₅ at low temperatures probe the nature of its magnetic-field-tuned QPT under the superconducting state. These studies detected the smeared jump-like behavior revealed both in the residual resistivity ρ_0 and the Hall resistivity R_H , along with the violation of the time invariance symmetry \mathcal{T} and the particle-hole symmetry \mathcal{C} . As a result, the studies provide vital clues on the nature of QPT taking place in CeCoIn₅ (see, e.g., [28,64,65]). Based on a number of experimental data, we show that observations point out unambiguously that the QPT of CeCoIn₅ is accompanied by the symmetry violation, and the QPT itself is represented by the topological FCQPT connecting two Fermi surfaces of different topological charges. We show that the behavior of CeCoIn₅ at the FCQPT in magnetic fields and under pressure is related to the flattening of the single-particle spectrum induced by the FCQPT that exerts profound effects on ρ_0 and the differential tunneling conductance in the normal state. The application of a magnetic field or pressure to CeCoIn₅ restores the Landau Fermi liquid behavior, leading to the suppression of both ρ_0 and the violation of \mathcal{T} and \mathcal{C} symmetries.

7.1. Residual Resistivity ρ_0

In the NFL state, the resistivity $\rho(T)$ is of the form

$$\rho(T) = \rho_0 + AT^n; \quad n = 1, \quad (22)$$

where ρ_0 is the residual resistivity, and A is a T -independent coefficient. The index n takes the values 1 and 2, respectively, for the NFL and LFL behaviors and $1 \lesssim n \lesssim 2$ in the NFL-LFL transition (see Figures 5, 12 and 13). The residual resistivity ρ_0 usually results from the scattering of impurities. At $T > T_c$, the zero-field resistivity $\rho(T, B = 0)$ varies linearly with T (see Equation (22)). At magnetic fields $B \geq B_{c2}$ and at low temperatures the resistivity exhibits LFL behavior, $\rho(T, B_{c2}) \propto T^2$. Experimentally, CeCoIn₅ is one of the purest heavy-fermion metals [65–68]. As a result, the regime of electron motion there is ballistic. Thus, under the application of the weak magnetic field B , one could observe a small positive contribution $\delta_B \propto B^2$ to ρ_0 arising from the orbital motion of electrons induced by the Lorentz force. As seen in Figure 12, this is not the case: specifically $\rho_0(B = B_{c0}) \simeq 3.0 \mu\Omega\text{cm}$ in the NFL state, while $\rho_0(B = 6\text{ T}) \simeq 0.3 \mu\Omega\text{cm}$ in the LFL state (see the inset to Figure 12) [65,68]. Moreover, it is seen in Figure 3 that at elevated temperatures, all the resistivities taken at different fields $B = 6, 10, 16\text{ T}$ tend to coincide at the NFL state with $\rho(T) \propto T$ since the contribution δ_B is relatively small.

Another direct experimental confirmation of the change in ρ_0 is obtained in measurements on CeCoIn₅ at various pressures P [69]. As seen in Figure 13, $\rho_0(P \rightarrow 0) \rightarrow 3.0 \mu\Omega\text{cm}$, and decreases by an order of magnitude to a value of about $\rho_0(P \rightarrow P^*) \rightarrow 0.2 \mu\Omega\text{cm}$, with $P^* \simeq 1.6\text{ GPa}$ [69]. Note that these values of the residual resistivity approximately coincide with those shown in Figure 12. Obviously, pressure P does not remove impurities from the sample. Thus, this large decrease in ρ_0 is due to the pressure-induced destruction of the FC state, as seen from the restoration of the LFL behavior at the same P^* . Similarly, the resistance $\rho(T, B)$ at fixed T as a function of B diminishes when the system transits from the NFL regime to the LFL regime under the application of magnetic field (the magnetoresistance becomes negative) [65]. This behavior is consistent with the FC theory [15]. Thus, the destruction of the FC state under the application of both magnetic fields B and pressure P entails a dramatic suppression of the flat band and its contribution to ρ_0 [32]. The same behavior of ρ_0 has been observed on twisted bilayer graphene, where a strong variation of ρ_0 is seen toward the magic angle [11,70]. In that case, the residual resistivity increases by

more than three orders of magnitude and resembles the behavior of ρ_0 shown in Figure 13. These observations are explained with the framework of the FC theory [27,32], and, to our best knowledge, have not found any different explanations.

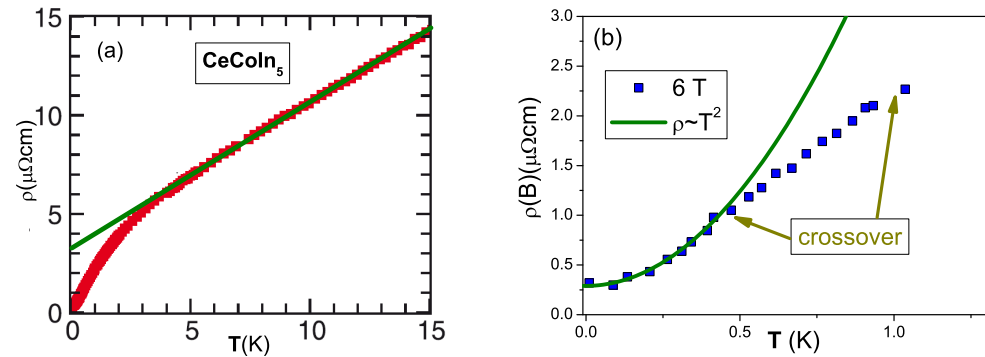


Figure 12. Resistivity $\rho(T, B)$ obtained in measurements on CeCoIn_5 under the application of magnetic fields B displayed in the legend [65]. The inset (a,b) shows both the LFL behavior of the resistivity at low temperatures and the crossover with $1 \lesssim n \lesssim 2$ at elevated T .

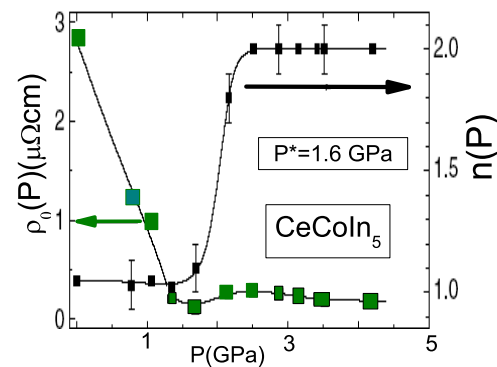


Figure 13. Adapted from [69]. Values of the residual resistivity ρ_0 (left axis, solid squares) and the index n in the fit $\rho(T) = \rho_0 + AT^n$ (right axis, solid squares) versus pressure P .

7.2. Asymmetric Tunneling Differential Conductivity

The particle–hole asymmetry is observed experimentally, analyzing the thermopower of HF compounds [43–45] (see Section 5). In this subsection, we continue to consider the particle–hole asymmetry taking place in HF compounds (see Section 4), and demonstrate that the differential tunneling conductivity (resistance) is an important instrument to explore the asymmetry in magnetic fields. The asymmetry takes place at a large scale of the universe [24], but here, we confine our consideration of HF compounds to illustrate the versatile and unique role of magnetic fields in analyzing the properties of HF compounds. Again, we shall see that the application of magnetic field makes the system transit from the NFL behavior to the LFL behavior (see Figures 2 and 11).

Consider the differential tunneling conductivity $\sigma_d(V)$ between an HF metal and a simple metallic point. At low temperatures, $\sigma_d(V)$ can be noticeably asymmetric with respect to the change in voltage bias V , which makes the asymmetric part $\Delta\sigma_d(V) = \sigma_d(V) - \sigma_d(-V)$ finite. The asymmetry can be observed in experiments on HF metals whose electronic system has undergone the topological FCQPT, while the application of magnetic field causes the system to exhibit the LFL behavior and eliminates the asymmetry, as it has been predicted [24,29]. Such behavior has been observed in measurements on the HF metal CeCoIn_5 [71], displayed in Figure 14. The data displayed in Figure 14 have been extracted from [71] (Figure S17) and demonstrate the sample independence of the asymmetry. As seen in Figure 14, $\Delta\sigma_d(V)$ is a linear function of V and vanishes in the presence of magnetic field at a sufficiently low temperature of 1.75 K [15,24,29,30]. We note that at

rising temperatures and fixed magnetic field B , the asymmetry emerges as soon as the NFL behavior again restores (see Figure 2a) since the elimination of the asymmetry is related to the crossover, rather than to a phase transition that takes place at finite temperature. We suggest that in the case of YbRh_2Si_2 at QCP tuned by the application of magnetic field, the asymmetry exhibits a jump as it does in the Hall coefficient. In the case of CeCoIn_5 , such a jump is absent since the corresponding QCP is hidden under the superconducting dome (see Section 7.3).

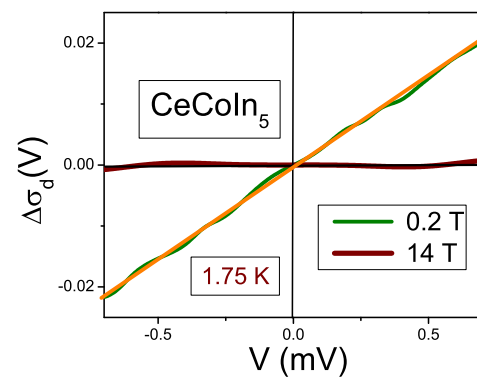


Figure 14. Asymmetric part $\Delta\sigma_d(V)$ of the tunneling differential conductivity measured on CeCoIn_5 and extracted from the experimental data [71]. Linear dependence of $\Delta\sigma_d$ is shown by the straight line. The asymmetric part disappears at $B = 14$ T and $T = 1.75$ K, with $B_{c0} \simeq 5$ T.

Now, we analyze how the asymmetrical part $\Delta\sigma_d(V)$ of the conductivity is related to the violation of \mathcal{T} and \mathcal{C} symmetries. Suppose we have a contact between HF and common metals. Let initially the electron current be directed from the HF metal to the usual metal. When voltage V is applied to the contact, we also change the electron charge $-e$ by $+e$, which changes the direction of the current. Consequently, one obtains exactly the above electric current under the voltage sign change $V \rightarrow -V$. As a result, the differential conductivity obtains the same asymmetric part $\Delta\sigma_d(V)$, as seen in Figure 14. If \mathcal{C} were conserved, the asymmetric part would vanish, $\Delta\sigma_d(V) = 0$. Thus, we conclude that because of the finite value of $\Delta\sigma_d(V)$, the \mathcal{C} symmetry is broken. In the same way, the time reversal $t \rightarrow -t$ for the constant charge generates the change in the current direction only. Since this reversal can also be achieved with $V \rightarrow -V$, it is clear that time-reversal symmetry is broken if $\Delta\sigma_d(V)$ is finite. Hence, both the \mathcal{C} and \mathcal{T} symmetries are violated, provided that the non-zero $\Delta\sigma_d(V) \neq 0$ emerges. In this case, the simultaneous transformation of $e \rightarrow -e$ and $t \rightarrow -t$ does not change anything, which means that the combined \mathcal{CT} symmetry is conserved. It is worth noting that in the present case, the coordinates reversal symmetry, the parity \mathcal{P} , is not violated so that the combined general \mathcal{CPT} symmetry is kept intact. It is well known that both \mathcal{C} and \mathcal{T} symmetries are preserved for systems of fermions described by the Landau theory. It follows that for such systems, as well as for ordinary metals, $\sigma_d(V)$ is a symmetric function of its variable V so that the conductivity asymmetry $\Delta\sigma_d(V)$ is not observed in them at low T (see, e.g., [15,24,29]). Thus, $\Delta\sigma_d(V) \neq 0$ signals the presence of FC and the corresponding flat band, which produce the violation of both \mathcal{T} and \mathcal{C} , as explained in Ref. [24]. It is seen in Figure 15 that in CeCoIn_5 , in both superconducting and the pseudogap state, the asymmetric tunneling conductivity rises, $\Delta\sigma_d(V) \neq 0$.

The data [72] displayed in Figure 15 are in good agreement with the data obtained in Ref. [73], as shown in Ref. [15]. These facts confirm that beyond B_{c0} , the FC state occurs, promoting both the superconducting and the corresponding pseudogap (PG) states [17]. As seen in Figure 15, at $T \leq 2.7$ the asymmetric tunneling conductivity $\Delta\sigma_d(V)$ is temperature independent. Such behavior is the intrinsic feature of HF metals located near the topological FCQPT [15]. This observation points to the fact that the PG state can be considered as the incoherent state emerging from the superconducting one. Thus, magnetic fields allow one to obtain unique information about the PG state.

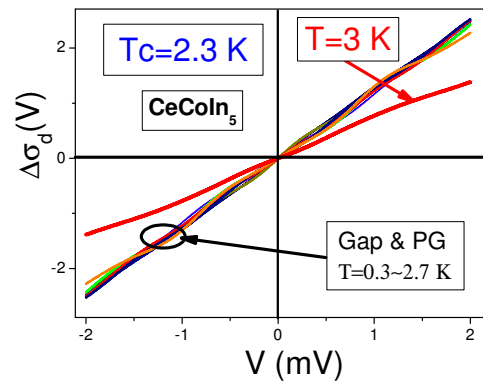


Figure 15. The asymmetric part of tunneling conductivity $\Delta\sigma_d(V)$ in CeCoIn_5 , extracted from the experimental data [72]. At $T \leq 2.7$ K CeCoIn_5 is in its pseudogap (PG) and superconducting states [72]. At $T \leq 2.7$ K, as it is shown by both the ring and the arrow, $\Delta\sigma_d(V)$ is temperature independent [15,17].

We note that, as predicted by [15,20,24,29], \mathcal{C} -symmetry violation in strongly correlated Fermi systems [43,45] has been experimentally observed. It is seen from the phase diagram in Figure 2 that at raising magnetic fields B and low temperatures T , the HF metal CeCoIn_5 exhibits LFL behavior and the symmetries are restored [24]. We note that the same behavior is exhibited by the HF metals YbRh_2Si_2 [74], $\text{YbCu}_{5-x}\text{Al}_x$ (for $x = 1.5$ [75]) and graphene [11], and explained within the framework of the FC theory [15]. We conclude that the phase transition in CeCoIn_5 is represented by the topological FCQPT and accompanied by the symmetry violation, as it does in the mentioned above HF metals such as the archetypal HF metal YbRh_2Si_2 (see Section 5) and graphene. We note that both \mathcal{C} and \mathcal{T} symmetries are violated due to the emergence of the flat band formed by the FC state (see Section 4). This observation is experimentally confirmed by the fact that the symmetries are restored under the application of magnetic field [15,24,29,75].

It is possible to measure the differential resistance dV/dI as a function of the current I . In fact, the symmetry properties of this function are the same as those of $\sigma_d(V)$: when a magnetic field is applied, the asymmetry of the differential resistance disappears since the system goes into the LFL state. Magnetic field dependence of the differential resistance dV/dI measured on graphene versus direct current I for different magnetic fields B is reported in Figure 16 [11]. Asymmetric part of the differential resistance $As(I) = dV/dI(I) - dV/dI(-I)$ decreases in an increased magnetic field and vanishes at $B \simeq 140$ mT, as can be seen in Figure 16. Such behavior is of great importance since the strongly correlated graphene has a perfect flat band [11]. Thus, in accordance with the prediction [15,29] the asymmetric part tends to zero at sufficiently high magnetic field, as seen in Figure 16. It is seen as well that the asymmetry remains at the superconducting state, and is suppressed at $B \simeq 140$ mT [24]. Thus, we can safely conclude that the strongly correlated state in graphene is controlled by the topological FCQPT, as it is in the HF compounds. To support our statement on the transition of graphene from the NFL behavior to the LFL, as it follows from vanishing the asymmetric part (see Figure 16), we predict that the resistance $\rho(T)$ versus T exhibits linear dependence, $\rho(T) \propto T$ in the normal state at zero magnetic field, while at relatively high magnetic fields and low temperatures of $k_B T \ll \mu_B B$ $\rho(T)$ exhibits $\rho(T) \propto T^2$ behavior, as it occurs in strongly correlated Fermi systems [15,16].

To conclude this subsection, we note that the violation of \mathcal{C} -symmetry in HF metals is directly sequestered with \mathcal{T} -symmetry violation. Meanwhile, the application of magnetic field B , driving the HF metal into its LFL state, restores both the \mathcal{T} and \mathcal{C} symmetries. One could suggest that the application of magnetic field is also to create the \mathcal{T} -symmetry violation. It is true, but the corresponding violation is rather weak in comparison with that induced by the presence of the flat band and needs special facilities to be observed.

Again, we have to stress the valuable role of magnetic fields in exploring the properties of HF compounds.

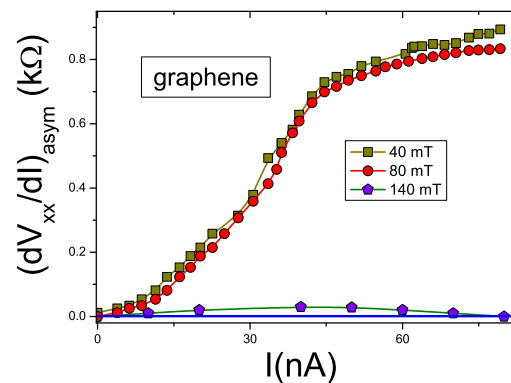


Figure 16. Magnetic field dependence of the asymmetric part $dV/dI(I) - dV/dI(-I)$ on the current I extracted from [11]. The different values of B are shown in the inset.

7.3. Hall Effect

We are now in a position to consider a possible jump in the Hall coefficient of the CeCoIn_5 at $B \rightarrow B_{c0}$ at the zero-temperature limit. Measurements of the Hall resistivity $R_H(T, B)$ in external magnetic fields B versus T have revealed a diverse low-temperature behavior of this basic property in HF metals, ranging from the LFL behavior to the challenging NFL one [28,31,33].

It is instructive to compare the behavior of the Hall coefficient in archetypal HF metals CeCoIn_5 and YbRh_2Si_2 . At $T \rightarrow 0$ in YbRh_2Si_2 , the application of the critical magnetic field B_{c0} suppressing the antiferromagnetic phase (with the Fermi momentum $p_{AF} \simeq p_F$) restores the LFL behavior with the Fermi momentum $p_f > p_F$, making an abrupt change in the Hall coefficient $R_H(T \rightarrow 0, B \rightarrow B_{c0})$, as a function of B [15,31,33]. At low temperatures and $B < B_{c0}$, the ground-state energy of the antiferromagnetic phase is lower than that of the heavy LFL, while at $B > B_{c0}$, the opposite happens, and the LFL state wins the competition. At $B = B_{c0}$, both the antiferromagnetic and the LFL states have the same ground-state energy. Thus, for $T = 0$ and $B = B_{c0}$, an infinitesimal change in the magnetic field B leads to a finite jump in the Fermi momentum (see the phase diagram in Figure 11). In response to this change, the Hall coefficient $R_H(B)$ experiences a corresponding sharp jump [15,31,33]. In the case of CeCoIn_5 , one can hardly expect to observe such a jump since the QCP is hidden under the superconducting dome (see the phase diagram Figure 2a). As a result, one can only observe $R_H(B > B_{c0})$. Measurements of the Hall coefficient on CeCoIn_5 do not show the possible jump, while the observed temperature dependence of $R_H(T, B)$ [28] can be explained within the framework of the FC theory [76]. The absence of the jump in the Hall coefficient could lead to the false impression that the quantum phase transition in CeCoIn_5 is not accompanied by the symmetry violation, but the study of the \mathcal{T} and \mathcal{C} symmetries and the change in the residual resistivity ρ_0 clearly signals that the violation of the symmetry does take place.

8. Summary

In our short review, we have analyzed the influence of magnetic field on the properties of strongly correlated heavy-fermion compounds such as heavy-fermion metals and frustrated insulators with quantum spin liquid. We have shown that the magnetic field B can be considered a universal tool, allowing one to explore the main properties of HF compounds. These properties are the T/B scaling, exhibiting under the application of magnetic field B at temperatures T and the emergence of the LFL behavior under the application of magnetic field. This emergence of the LFL behavior is accompanied by the restoration of the \mathcal{T} and \mathcal{C} symmetries and by the decrease of the residual resistivity ρ_0 .

We have revealed and explained the universal scaling of the thermopower S/T in such different HF compounds as YbRh_2Si_2 , $\beta\text{-YbAlB}_4$, and $[\text{BiBa}_{0.66}\text{K}_{0.36}\text{O}_2]\text{CoO}_2$. Our calculations are in good agreement with observations and show that the promoted universal S/T scaling actually takes place. This scaling does not depend on the specific properties of the HF compounds under consideration and coincides with the scaling of the normalized effective mass $M_N^* = (C/T)_N$, i.e., it is a scaling characteristic of HF compounds. We have also shown that destruction of the flattening of the single-particle spectrum profoundly affects S/T , eliminates the particle asymmetry, and leads to the two jumps and to the change of sign of the thermopower occurring at the antiferromagnetic phase transition.

We have delineated the quantum phase transition in CeCoIn_5 , and explained a number of experimental data collected in measurements on CeCoIn_5 that allowed us to clarify the corresponding quantum phase transition. We have shown that the data related to the behavior under the application of magnetic fields of both the residual resistivity and the asymmetrical tunneling conductivity clearly point to the symmetry violation occurring at the quantum phase transition in CeCoIn_5 . From the experimental point of view, we have shown that these data demonstrate that the quantum phase transition in CeCoIn_5 is accompanied by the symmetry breaking related to the violation of the \mathcal{T} and \mathcal{C} symmetries, and is represented by the topological FCQPT that connects two Fermi surfaces of different topological charges, as it occurs in graphene and the archetypal HF metal YbRh_2Si_2 . We have explained why the Hall coefficient does not exhibit the jump at the phase transition in CeCoIn_5 , as it does in the case of YbRh_2Si_2 .

Finally, our explanation of the number of experimental results within the framework of the fermion condensation theory suggests that the topological FCQPT is the intrinsic feature of many strongly correlated Fermi systems. This topological phase transition can be viewed as the universal cause for the non-Fermi liquid behavior and for the existence of the new state of matter represented by the strongly correlated Fermi systems (see, e.g., [15–17,24]).

Author Contributions: V.R.S. and A.Z.M. designed the project and directed it with the help of S.A.A., S.A.A. performed the calculations. V.R.S. and A.Z.M. wrote the manuscript and all authors commented on it. The manuscript reflects the contributions of all authors. All authors have read and agreed to the published version of the manuscript.

Funding: This research received no external funding.

Acknowledgments: We thank V.A. Khodel for fruitful discussions. This work was supported by U.S. DOE, Division of Chemical Sciences, Office of Basic Energy Sciences, Office of Energy Research, AFOSR.

Conflicts of Interest: The authors declare no conflict of interest.

References

1. Landau, L.D. Theory of Fermi liquid. *Sov. Phys. JETP* **1956**, *30*, 920 .
2. Lifshitz, E.M.; Pitaevskii, L.P. *Statistical Physics, Part 2*; Butterworth-Heinemann: Oxford, UK, 1999.
3. Abrikosov, A.A. *Fundamentals of the Theory of Metals*; North-Holland: Amsterdam, The Netherlands, 1988.
4. Senthil, T.; Vojta, M.; Sachdev, S. Weak magnetism and non-Fermi liquids near heavy-fermion critical points. *Phys. Rev. B* **2004**, *69*, 035111. [[CrossRef](#)]
5. Coleman, P.; Schofield, A.J. Quantum criticality. *Nature* **2005**, *433*, 226. [[CrossRef](#)] [[PubMed](#)]
6. Coleman, P.; Pèpin, C.; Si, Q.; Ramazashvili, R. How do Fermi liquids get heavy and die? *J. Phys. Condens. Matter* **2001**, *13*, R723. [[CrossRef](#)]
7. Löhneysen, H.V.; Rosch, A.; Vojta, M.; Wölfle, P. Fermi-Liquid Instabilities at Magnetic Quantum Phase Transitions. *Rev. Mod. Phys.* **2007**, *79*, 1015. [[CrossRef](#)]
8. Gegenwart, P.; Si, Q.; Steglich, F. Quantum criticality in heavy-fermion metals. *Nat. Phys.* **2008**, *4*, 186. [[CrossRef](#)]
9. Stockert, O.; Steglich, F. Unconventional Quantum Criticality in Heavy-Fermion Compounds. *Annu. Rev. Condens. Matter Phys.* **2011**, *2*, 79. [[CrossRef](#)]
10. Sachdev, S. Quantum magnetism and criticality. *Nat. Phys.* **2008**, *4*, 173. [[CrossRef](#)]
11. Cao, Y.; Fatemi, V.; Fang, S.; Watanabe, K.; Taniguchi, T.; Kaxiras, E.; Jarillo-Herrero, P. Unconventional superconductivity in magic-angle graphene superlattices. *Nature* **2018**, *556*, 43–50. [[CrossRef](#)]

12. Törmä, P.; Peotta, S.; Bernevig, B.A. Superconductivity, superfluidity and quantum geometry in twisted multilayer systems. *Nat. Rev. Phys.* **2022**, *4*, 528. [[CrossRef](#)]
13. Regnault, N.; Xu, Y.; Li, M.-R.; Ma, D.-S.; Jovanovic, M.; Yazdani, A.; Parkin, S.S.P.; Felser, C.; Schoop, L.M.; Ong, N.P.; et al. Catalogue of flat-band stoichiometric materials. *Nature* **2022**, *603*, 824. [[CrossRef](#)]
14. Shaginyan, V.R.; Msezane, A.Z.; Popov, K.G.; Stephanovich, V.A. Universal Behavior of Two-Dimensional He 3 at Low Temperatures. *Phys. Rev. Lett.* **2008**, *100*, 096406. [[CrossRef](#)] [[PubMed](#)]
15. Shaginyan, V.R.; Amusia, M.Y.; Msezane, A.Z.; Popov, K.G. Scaling behavior of heavy fermion metals. *Phys. Rep.* **2010**, *492*, 31. [[CrossRef](#)]
16. Amusia, M.Y.; Popov, K.G.; Shaginyan, V.R.; Stephanovich, V.A. *Theory of Heavy-Fermion Compounds*; Springer Series in Solid-State Sciences; Springer: Heidelberg, Germany; New York, NY, USA; Dordrecht, The Netherlands; London, UK, 2015; Volume 182.
17. Amusia, M.Y.; Shaginyan, V.R. *Strongly Correlated Fermi Systems: A New State of Matter*; Springer Tracts in Modern Physics; Springer Nature: Cham, Switzerland, 2020; Volume 283.
18. Khodel, V.A.; Shaginyan, V. Superfluidity in system with fermion condensate. *J. Exp. Theor. Phys. Lett.* **1990**, *51*, 553.
19. Volovik, G.E. A new class of normal Fermi liquids. *J. Exp. Theor. Phys. Lett.* **1991**, *53*, 222.
20. Khodel, V.A.; Shaginyan, V.R.; Khodel, V.V. New approach in the microscopic Fermi systems theory. *Phys. Rep.* **1994**, *249*, 1. [[CrossRef](#)]
21. Volovik, G.E. From Standard Model of particle physics to room-temperature superconductivity. *Phys. Scr.* **2015**, *164*, 014014. [[CrossRef](#)]
22. Volovik, G.E. *Springer Lecture Notes in Physics*; Springer: Berlin/Heidelberg, Germany, 2007; Volume 718, p. 31.
23. Khodel, V.A.; Clark, J.W.; Zverev, M.V. Topology of the Fermi surface beyond the quantum critical point. *Phys. Rev.* **2008**, *78*, 075120. [[CrossRef](#)]
24. Shaginyan, V.R.; Msezane, A.Z.; Japaridze, G.S.; Stephanovich, V.A. Violation of the Time-Reversal and Particle-Hole Symmetries in Strongly Correlated Fermi Systems: A Review. *Symmetry* **2020**, *12*, 1596. [[CrossRef](#)]
25. Clark, J.W.; Khodel, V.A.; Zverev, M.V. Anomalous low-temperature behavior of strongly correlated Fermi systems. *Phys. Rev.* **2005**, *71*, 012401. [[CrossRef](#)]
26. Kadowaki, K.; Woods, S.B. Universal relationship of the resistivity and specific heat in heavy-Fermion compounds. *Solid State Commun.* **1986**, *58*, 507. [[CrossRef](#)]
27. Khodel, V.A.; Clark, J.W.; Zverev, M.V. Topological disorder triggered by interaction-induced flattening of electron spectra in solids. *Phys. Rev.* **2020**, *102*, 201108(R). [[CrossRef](#)]
28. Maksimovic, N.; Eilbott, D.H.; Cookmeyer, T.; Wan, F.; Rusz, J.; Nagarajan, V.; Haley, S.C.; Maniv, E.; Gong, A.; Faubel, S.; et al. Evidence for a delocalization quantum phase transition without symmetry breaking in CeCoIn₅. *Science* **2022**, *375*, 76. [[CrossRef](#)] [[PubMed](#)]
29. Shaginyan, V.R. Dissymmetrical tunnelling in heavy fermion metals. *J. Exp. Theor. Phys. Lett.* **2005**, *81*, 222. [[CrossRef](#)]
30. Shaginyan, V.R.; Msezane, A.Z.; Japaridze, G.S. Peculiar Physics of Heavy-Fermion Metals: Theory versus Experiment. *Atoms* **2022**, *10*, 67. [[CrossRef](#)]
31. Shaginyan, V.R.; Popov, P.G.; Artamonov, S.A. Hall coefficient in heavy fermion metals. *J. Exp. Theor. Phys. Lett.* **2005**, *82*, 215. [[CrossRef](#)]
32. Shaginyan, V.R.; Msezane, A.Z.; Popov, K.G.; Clark, J.W.; Zverev, M.V.; Khodel, V.A. Magnetic field dependence of the residual resistivity of the heavy-fermion metal CeCoIn₅. *Phys. Rev. B* **2012**, *86*, 085147. [[CrossRef](#)]
33. Paschen, S.; Lüthmann, T.; Wirth, S.; Gegenwart, P.; Trovarelli, O.; Geibel, C.; Steglich, F.; Coleman, P.; Si, Q. Hall-effect evolution across a heavy-fermion quantum critical point. *Nature* **2004**, *432*, 881. [[CrossRef](#)]
34. Chen, Q.Y.; Xu, D.F.; Niu, X.H.; Jiang, J.; Peng, R.; Xu, H.C.; Wen, C.H.P.; Ding, Z.F.; Huang, K.; Shu, L.; et al. Direct observation of how the heavy-fermion state develops in CeCoIn₅. *Phys. Rev.* **2017**, *96*, 045107. [[CrossRef](#)]
35. Pfitzner, M.; Wölfle, P. Quasiparticle interaction in a nearly localized Fermi liquid: Application to ³He and heavy-fermion systems. *Phys. Rev. B* **1986**, *33*, 2003. [[CrossRef](#)]
36. Oliveira, L.N.; Gross, E.K.U.; Kohn, W. Density-functional theory for superconductors. *Phys. Rev. Lett.* **1988**, *60*, 2430. [[CrossRef](#)]
37. Shaginyan, V.R. Density functional theory of fermion condensation. *Phys. Lett. A* **1998**, *249*, 237. [[CrossRef](#)]
38. Oeschler, N.; Hartmann, S.; Pikul, A.; Krellner, C.; Geibel, C.; Steglich, F. Low-temperature specific heat of YbRh₂Si₂. *Physica B* **2008**, *403*, 1254. [[CrossRef](#)]
39. Tokiwa, Y.; Radu, T.; Geibel, C.; Steglich, F.; Gegenwart, P. Divergence of magnetic Grüneisen ratio at the field-induced quantum critical point in YbRh₂Si₂. *Phys. Rev. Lett.* **2009**, *102*, 066401. [[CrossRef](#)] [[PubMed](#)]
40. Schröder, A.; Aeppli, G.; Coldea, R.; Adams, M.; Stockert, O.; Löhneysen, H.V.; Bucher, E.; Ramazashvili, R.; Coleman, P. Onset of antiferromagnetism in heavy-fermion metals. *Nature* **2000**, *407*, 351. [[CrossRef](#)] [[PubMed](#)]
41. Helton, J.S.; Matan, K.; Shores, M.P.; Nytko, E.A.; Bartlett, B.M.; Qiu, Y.; Nocera, D.G.; Lee, Y.S. Dynamic Scaling in the Susceptibility of the Spin-1/2 Kagome Lattice Antiferromagnet Herbertsmithite. *Phys. Rev. Lett.* **2010**, *104*, 147201. [[CrossRef](#)]
42. Murayama, H.; Tominaga, T.; Asaba, T.; Silva, A.O.; Sato, Y.; Suzuki, H.; Ukai, Y.; Suetsugu, S.; Kasahara, Y.; Okuma, R.; et al. Universal scaling of specific heat in the S=1/2 quantum kagome antiferromagnet herbertsmithite. *Phys. Rev. B* **2022**, *106*, 174406. [[CrossRef](#)]

43. Gourgout, A.; Grissonnanche, G.; Lalibertè, F.; Ataei, A.; Chen, L.; Verret, S.; Zhou, J.-S.; Mravlje, J.; Georges, A.; Doiron-Leyraud, N.; et al. Seebeck Coefficient in a Cuprate Superconductor: Particle-Hole Asymmetry in the Strange Metal Phase and Fermi Surface Transformation in the Pseudogap Phase. *Phys. Rev. X* **2022**, *12*, 011037. [[CrossRef](#)]
44. Paul, A.K.; Ghosh, A.; Chakraborty, S.; Roy, U.; Dutta, R.; Watanabe, K.; Taniguchi, T.; Panda, A.; Agarwala, A.; Mukerjee, S.; et al. Interaction-driven giant thermopower in magic-angle twisted bilayer graphene. *Nat. Phys.* **2022**, *18*, 691. [[CrossRef](#)]
45. Stepanov, P. Thermopower probes electronic flat bands. *Nat. Phys.* **2022**, *18*, 608. [[CrossRef](#)]
46. Hartmann, S.; Oeschler, N.; Krellner, C.; Geibel, C.; Paschen, S.; Steglich, F. Thermopower Evidence for an Abrupt Fermi Surface Change at the Quantum Critical Point of YbRh_2Si_2 . *Phys. Rev. Lett.* **2010**, *104*, 096401. [[CrossRef](#)]
47. Friedemann, S.; Wirth, S.; Kirchner, S.; Si, Q.; Hartmann, S.; Krellner, C.; Geibel, C.; Westerkamp, T.; Brando, M.; Steglich, F. Break Up of Heavy Fermions at an Antiferromagnetic Instability. *J. Phys. Soc. Jpn.* **2011**, *80*, SA002. [[CrossRef](#)]
48. Kim, K.-S.; Pépin, C. Thermopower as a signature of quantum criticality in heavy fermions. *Phys. Rev.* **2010**, *81*, 205108. [[CrossRef](#)]
49. Kim, K.-S.; Pépin, C. Thermopower as a fingerprint of the Kondo breakdown quantum critical point. *Phys. Rev.* **2011**, *83*, 073104. [[CrossRef](#)]
50. Lifshitz, E.M.; Landau, L.D.; Pitaevskii, L.P. *Electrodynamics of Continuous Media*; Elsevier: New York, NY, USA, 1984.
51. Behnia, K.; Jaccard, D.; Flouquet, J. On the thermoelectricity of correlated electrons in the zero-temperature limit. *J. Phys. Condens. Matt.* **2004**, *16*, 5187. [[CrossRef](#)]
52. Miyake, K.; Kohno, H. Theory of Quasi-Universal Ratio of Seebeck Coefficient to Specific Heat in Zero-Temperature Limit in Correlated Metals. *J. Phys. Soc. Jpn.* **2005**, *74*, 254. [[CrossRef](#)]
53. Zlatić, V.; Monnier, R.; Freericks, J.K.; Becker, K.W. Relationship between the thermopower and entropy of strongly correlated electron systems. *Phys. Rev.* **2007**, *76*, 085122. [[CrossRef](#)]
54. Shaginyan, V.R.; Msezane, A.Z.; Japaridze, G.S.; Popov, K.G.; Clark, J.W.; Khodel, V.A. Scaling behavior of the thermopower of the archetypal heavy-fermion metal YbRh_2Si_2 . *Front. Phys.* **2016**, *11*, 117102. [[CrossRef](#)]
55. Nozières, P. Properties of Fermi liquids with a finite range interaction. *J. Phys.* **1992**, *2*, 443. [[CrossRef](#)]
56. Limelette, P.; Saulquin, W.; Muguerra, H.; Grebille, D. From quantum criticality to enhanced thermopower in strongly correlated layered cobalt oxide. *Phys. Rev.* **2010**, *81*, 115113. [[CrossRef](#)]
57. Gegenwart, P.; Custers, J.; Geibel, C.; Neumaier, K.; Tayama, T.; Tenya, K.; Trovarelli, O.; Steglich, F. Magnetic-Field Induced Quantum Critical Point in YbRh_2Si_2 . *Phys. Rev. Lett.* **2002**, *89*, 056402. [[CrossRef](#)] [[PubMed](#)]
58. Mokashi, A.; Li, S.; Wen, B.; Kravchenko, S.V.; Shashkin, A.A.; Dolgoplov, V.T.; Sarachik, M.P. Critical Behavior of a Strongly Interacting 2D Electron System. *Phys. Rev. Lett.* **2012**, *109*, 096405. [[CrossRef](#)] [[PubMed](#)]
59. Machida, Y.; Tomokuni, K.; Ogura, C.; Izawa, K.; Kuga, K.; Nakatsuji, S.; Lapertot, G.; Knebel, G.; Brison, J.-P.; Flouquet, J. Thermoelectric Response Near a Quantum Critical Point of YbAlB_4 and YbRh_2Si_2 : A Comparative Study. *Phys. Rev. Lett.* **2012**, *109*, 156405. [[CrossRef](#)] [[PubMed](#)]
60. Taupin, M.; Paschen, S. Are Heavy Fermion Strange Metals Planckian? *Crystals* **2022**, *12*, 251. [[CrossRef](#)]
61. Köhler, U.; Oeschler, N.; Steglich, F.; Maquilon, S.; Fisk, Z. Energy scales of $\text{Lu}_{1-x}\text{Yb}_x\text{Rh}_2\text{Si}_2$ by means of thermopower investigations. *Phys. Rev.* **2008**, *77*, 104412. [[CrossRef](#)]
62. Lifshitz, E.M.; Pitaevskii, L.P. *Statistical Physics, Part 1*; Butterworth-Heinemann: Oxford, UK, 1996.
63. Krellner, C.; Hartmann, S.; Pikul, A.; Oeschler, N.; Donath, J.G.; Geibel, C.; Steglich, F.; Wosnitza, J. Violation of Critical Universality at the Antiferromagnetic Phase Transition of YbRh_2Si_2 . *Phys. Rev. Lett.* **2009**, *102*, 196402. [[CrossRef](#)]
64. Bianchi, A.; Movshovich, R.; Oeschler, N.; Gegenwart, P.; Steglich, F.; Thompson, J.D.; Pagliuso, P.G.; Sarrao, J.L. First-Order Superconducting Phase Transition in CeCoIn_5 . *Phys. Rev. Lett.* **2002**, *89*, 137002. [[CrossRef](#)]
65. Paglione, J.; Tanatar, M.; Hawthorn, D.G.; Boaknin, E.; Hill, R.W.; Ronning, F.; Sutherland, M.; Taillefer, L.; Petrovic, C.; Canfield, P.C. Field-induced quantum critical point in CeCoIn_5 . *Phys. Rev. Lett.* **2003**, *91*, 246405. [[CrossRef](#)]
66. Seyfarth, G.; Brison, J.P.; Knebel, G.; Aoki, D.; Lapertot, G.; Flouquet, J. Multigap Superconductivity in the Heavy-Fermion System CeCoIn_5 . *Phys. Rev. Lett.* **2008**, *101*, 046401. [[CrossRef](#)]
67. Tokiwa, Y.; Bauer, E.D.; Gegenwart, P. Zero-Field Quantum Critical Point in CeCoIn_5 . *Phys. Rev. Lett.* **2013**, *111*, 107003. [[CrossRef](#)]
68. Paglione, J.; Tanatar, M.A.; Hawthorn, D.G.; Ronning, F.; Hill, R.W.; Sutherland, M.; Taillefer, L.; Petrovic, C. Nonvanishing energy scales at the quantum critical point of CeCoIn_5 . *Phys. Rev. Lett.* **2006**, *97*, 106606. [[CrossRef](#)] [[PubMed](#)]
69. Sidorov, V.A.; Nicklas, M.; Pagliuso, P.G.; Sarrao, J.L.; Bang, Y.; Balatsky, A.V.; Thompson, J.D. Superconductivity and quantum criticality in CeCoIn_5 . *Phys. Rev. Lett.* **2002**, *89*, 157004. [[CrossRef](#)] [[PubMed](#)]
70. Polshyn, H.; Yankowitz, M.; Chen, S.; Zhang, Y.; Watanabe, K.; Taniguchi, T.; Dean, C.R.; Young, A.F. Large linear-in-temperature resistivity in twisted bilayer graphene. *Nat. Phys.* **2019**, *15*, 1011. [[CrossRef](#)]
71. Shrestha, K.; Zhang, S.; Greene, L.H.; Lai, Y.; Baumbach, R.E.; Sasmal, K.; Maple, M.B.; Park, W.K. Spectroscopic evidence for the direct involvement of local moments in the pairing process of the heavy-fermion superconductor CeCoIn_5 . *Phys. Rev.* **2021**, *103*, 224515. [[CrossRef](#)]
72. Wirth, S.; Prots, Y.; Wedel, M.; Ernst, S.; Kirchner, S.; Fisk, Z.; Thompson, J.D.; Steglich, F.; Grin, Y. J. Structural Investigations of CeIrIn_5 and CeCoIn_5 on Macroscopic and Atomic Length Scales. *Phys. Soc. Jpn.* **2014**, *83*, 061009. [[CrossRef](#)]
73. Park, W.K.; Greene, L.H.; Sarrao, J.L.; Thompson, J.D. Andreev reflection at the normal-metal/heavy-fermion superconductor CeCoIn_5 interface. *Phys. Rev. B* **2005**, *72*, 052509. [[CrossRef](#)]

74. Seiro, S.; Jiao, L.; Kirchner, S.; Hartmann, S.; Friedemann, S.; Krellner, C.; Geibel, C.; Si, Q.; Steglich, F.; Wirth, S. Evolution of the Kondo lattice and non-Fermi liquid excitations in a heavy-fermion metal. *Nat. Commun.* **2018**, *9*, 3324. [[CrossRef](#)]
75. Pristāš, G.; Reiffers, M.; Bauer, E.; Jansen, A.G.M.; Maude, D.K. Suppression of asymmetric differential resistance in the non-Fermi-liquid system $\text{YbCu}_{5-x}\text{Al}_x$ ($x = 1.3\text{--}1.75$) in high magnetic fields. *Phys. Rev. B* **2008**, *78*, 235108. [[CrossRef](#)]
76. Khodel, V.A.; Zverev, M.V.; Clark, J.W. Damping effects and the metal-insulator transition in the two-dimensional electron gas. *J. Exp. Theor. Phys. Lett.* **2005**, *81*, 315. [[CrossRef](#)]

Disclaimer/Publisher's Note: The statements, opinions and data contained in all publications are solely those of the individual author(s) and contributor(s) and not of MDPI and/or the editor(s). MDPI and/or the editor(s) disclaim responsibility for any injury to people or property resulting from any ideas, methods, instructions or products referred to in the content.